

# A Hybrid Iterative Numerical Transferable Solver (HINTS) for PDEs Based on Deep Operator Network and Relaxation Methods

Enrui Zhang<sup>a\*</sup>, Adar Kahana<sup>a\*</sup>, Eli Turkel<sup>b</sup>, Rishikesh Ranade<sup>c</sup>, Jay Pathak<sup>c</sup>, George Em Karniadakis<sup>ad\*\*</sup>

<sup>a</sup>*Division of Applied Mathematics, Brown University, Providence, RI 02912, USA*

<sup>b</sup>*Department of Applied Mathematics, Tel Aviv University, Tel Aviv 69978, Israel*

<sup>c</sup>*CTO Office, Ansys Inc, Canonsburg, PA 15317, USA*

<sup>d</sup>*School of Engineering, Brown University, Providence, RI 02912, USA*

---

## Abstract

Iterative solvers of linear systems are a key component for the numerical solutions of partial differential equations (PDEs). While there have been intensive studies through past decades on classical methods such as Jacobi, Gauss-Seidel, conjugate gradient, multigrid methods and their more advanced variants, there is still a pressing need to develop faster, more robust and reliable solvers. Based on recent advances in scientific deep learning for operator regression, we propose HINTS, a hybrid, iterative, numerical, and transferable solver for differential equations. HINTS combines standard relaxation methods and the Deep Operator Network (DeepONet). Compared to standard numerical solvers, HINTS is capable of providing faster solutions for a wide class of differential equations, while preserving the accuracy close to machine zero. Through an eigenmode analysis, we find that the individual solvers in HINTS target distinct regions in the spectrum of eigenmodes, resulting in a uniform convergence rate and hence exceptional performance of the hybrid solver overall. Moreover, HINTS applies to equations in multidimensions, and is flexible with regards to computational domain and transferable to different discretizations.

---

\*Authors contributed equally

\*\*Corresponding author E-mail: george.karniadakis@brown.edu

## 1. Introduction

Since the proposal of numerical methods for solving differential equations more than half a century ago, scientists and engineers have been able to significantly expand knowledge and insights that have never been achieved in the analytical era, in all fields of physical sciences and engineering [1, 2] such as astrophysics [3], quantum physics [4], fluid dynamics [5, 6, 7], solid mechanics [8, 9, 10, 11], material science [12], and electrodynamics [13]. With an appropriate numerical method such as finite differences [14], finite elements [8, 15], or a spectral method [16], one may obtain the solution of differential equations that may involve nonlinearity, complex geometry, and/or multiscale phenomena. Thus, one acquires a quantitative knowledge and understanding of the governing mechanism of physical and engineering systems.

Despite the diversity of differential equations in different areas, their numerical solutions, in many cases, are reduced to solving systems of linear equations as the last step. This seemingly simple task is, however, not perfectly resolved yet so far. Existing numerical solvers are frequently convergent and stable only for linear systems satisfying certain conditions (e.g., positive definiteness) [17]. Computational efficiency becomes an issue when dealing with large-scale systems. Among the iterative solvers, the Jacobi method and the Gauss-Seidel method (see a brief review in Section S1 in Supplementary Information (SI)), as the most classical methods, suffer from divergence for non-symmetric and indefinite systems and slow convergence associated with low-frequency eigenmodes. More advanced iterative methods [18, 19, 20, 21, 22, 23, 24, 25, 26, 27, 28] and techniques have been proposed to mitigate these two issues. In particular, multigrid methods [27, 28, 29, 30, 31, 32, 33, 34] (see Section S1 in SI) use a hierarchy of discretizations to efficiently relax eigenmodes of all frequencies, making them one of the state-of-the-art methods in terms of computational efficiency. Despite being a century-old problem, solving linear systems is still an open question, calling for better algorithms that are more efficient and applicable to broader classes of linear systems.

In the recent decade, scientific machine learning (SciML) has developed rapidly for problems in physical sciences and engineering due to its prominent advantage in predictive capability and efficiency. In particular, deep learning for operator regression is an active research area of wide interest and substantial importance. Recent works have proposed several frameworks, including the deep operator network (DeepONet) [35], Fourier Neural Operator (FNO) [36], etc. [37, 38]. Among these methods, DeepONet was the original method and was proposed based on the universal approximation theorem for operators [39], showing a strong prediction capability in diverse engineering fields [40, 41, 42, 43, 44, 45, 46, 47, 48, 49] (see a brief review in Section S2 in SI). It provides fast inference for mappings between functions, which can be highly nonlinear and may take hours or even days to simulate using traditional approaches.

In some SciML works, researchers introduce learning algorithms into numerical solvers for differential equations and/or their associated linear systems. Briefly, these works seek to replace and/or improve existing numerical solvers. Physics-informed neural networks [50, 51, 52, 53, 54, 55, 56] and related works [57, 58] represent a unique methodology where the differential equation is explicitly encoded into the loss function, hence entirely eliminating the needs to employ numerical solvers during both training and testing stages. Among the majority of studies without such explicit encoding, a deep learning model needs to be trained with sufficient data, typically acquired from numerical solvers. Once the training completes, it provides fast and approximate predictions without invoking numerical solvers [59, 60, 61, 62, 63, 64, 65]. Many other studies focus on improvements on top of numerical solvers, such as: a correction on coarse-grid results [66], a better iterative scheme [67, 68, 69], a better initial guess of the solution [70], a better meshing strategy [71, 72], a better discretization operator [73], a better prolongator/restrictor [74, 75] or a preconditioner [76] for multigrid methods.

In this paper, we propose a fundamentally different approach to integrate DeepONet and standard relaxation methods, yielding HINTS – a hybrid, iterative, numerical, and

transferable solver for differential equations. Our objective is to utilize the merits from both sides to design a fast, accurate, and widely applicable solver for differential equations. We demonstrate the effectiveness of HINTS and analyze its characteristics by presenting a series of numerical examples, including different choices of integrated standard solvers and differential equations with different characteristics, varying spatial geometries, and multidimensions.

## 2. Results

### 2.1. Formulating HINTS by Integrating DeepONet and Relaxation Solvers

For the scope of this study, we consider the following linear differential equation

$$\mathcal{L}_{\mathbf{x}}(u; k) = f, \mathbf{x} \in \Omega \quad (1a)$$

$$\mathcal{B}_{\mathbf{x}}(u) = g, \mathbf{x} \in \partial\Omega \quad (1b)$$

where  $\mathcal{L}_{\mathbf{x}}$  is the differential operator,  $\mathcal{B}_{\mathbf{x}}$  is the boundary operator,  $k = k(\mathbf{x})$  parameterizes  $\mathcal{L}_{\mathbf{x}}$ ,  $f = f(\mathbf{x})$  and  $g = g(\mathbf{x})$  are the right-hand-side forcing terms, and  $u = u(\mathbf{x})$  is the solution. Assuming that  $g$  is a known fixed function, Eq. 1 defines a family of differential equations parameterized by  $f$  and  $k$ .

Before employing HINTS, we first need to train a DeepONet offline. This DeepONet approximates the solution operator  $\mathcal{G}$  defined by

$$\mathcal{G} : k, f \mapsto u \text{ s.t. Eq. 1 holds,} \quad (2)$$

where we have assumed the uniqueness of the solution  $u$ . DeepONet receives  $k(x)$  and  $f(x)$  in the form of discrete evaluations on  $n_D + 1$  uniform points, respectively. We denote this discretization associated with DeepONet as  $\Omega^{h_D}$ . More details of the setup of the DeepONet are included in Methods and Section S3 in SI.

The workflow of a general HINTS is shown in Fig. 1. After discretizing the differential equation into linear systems, traditional solvers adopt a fixed relaxation method in each

iteration. HINTS, on the other hand, creates a second branch of the iterator using a trained DeepONet. During the process of the iterative solution, we alternately adopt the numerical iterator and the DeepONet iterator with ratio 1 :  $(n_r - 1)$  (i.e., DeepONet with proportion  $1/n_r$ ), until the solution converges. The numerical iterator may be chosen from established solvers, such as the Jacobi method, the Gauss-Seidel method, and the multigrid method, etc.

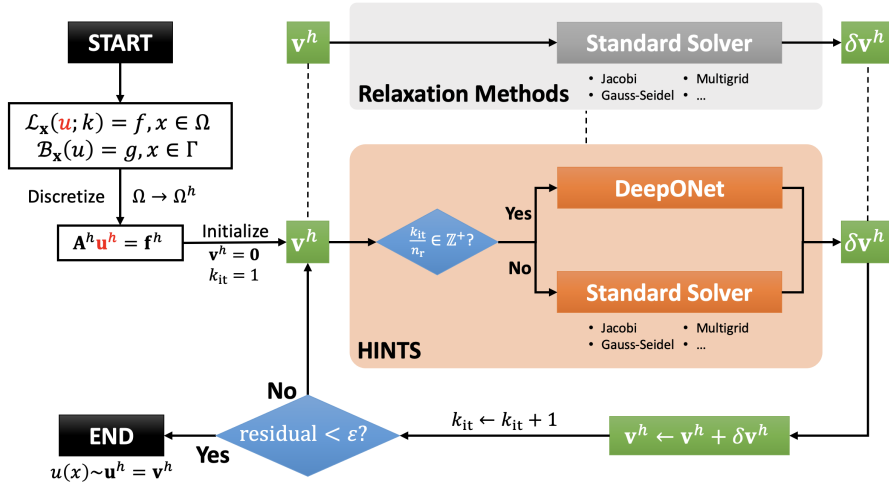


Figure 1: **Overview of the Hybrid Iterative Numerical Transferable Solver (HINTS)**. The goal is to solve  $u(\mathbf{x})$  in the differential equation. HINTS start by discretizing the computational domain  $\Omega$  into  $\Omega^h$  and initializing a guess of the solution ( $\mathbf{v}^h = 0$ , for example). In the  $k_{it}$ th iteration, the approximate solution  $\mathbf{v}^h$  is corrected by  $\delta\mathbf{v}^h$  through either the DeepONet solver or the standard numerical solver. The choice of the solver is determined by whether  $n_r$  divides  $k_{it}$ , where  $n_r$  is a parameter that we choose to optimize the performance. There is a plurality of choices for the numerical solver, such as Jacobi, Gauss-Seidel, and multigrid methods. The algorithm proceeds until the residual of  $\mathbf{v}^h$  is smaller than a threshold  $\varepsilon$ .

Among the choices of the numerical iterators, we mainly consider the (damped) Jacobi method, formulating the HINTS-Jacobi algorithm (see pseudo-code in Section S3 in SI). For a class of equations defined by Eq. 1, the target is to compute the solution  $u(\mathbf{x})$  given  $k(\mathbf{x})$  and  $f(\mathbf{x})$ . The algorithm starts by discretizing the domain  $\Omega$  into  $\Omega^h$  and assembling the  $n$ -dimensional linear system  $\mathbf{A}^h \mathbf{u}^h = \mathbf{f}^h$ . In each iteration, given the

previous approximate solution  $\mathbf{v}^h$  ( $\approx \mathbf{u}^h$ ), the algorithm seeks to solve  $\delta\mathbf{v}^h$  in  $\mathbf{A}^h\delta\mathbf{v}^h = \mathbf{r}^h$ , where  $\mathbf{r}^h$  is current residual of the system defined by

$$\mathbf{r}^h := \mathbf{f}^h - \mathbf{A}^h\mathbf{v}^h, \quad (3)$$

and then make a correction to the previous  $\mathbf{v}^h$  by  $\mathbf{v}^h \leftarrow \mathbf{v}^h + \delta\mathbf{v}^h$ . To calculate the correction  $\delta\mathbf{v}^h$ , either DeepONet or the Jacobi solver is invoked. For the DeepONet solver, it takes  $k(\mathbf{x})$  and  $r(\mathbf{x})$  (function-form residual corresponding to the vector-form  $\mathbf{r}^h$ ) as inputs, and yields  $v(\mathbf{x}) = \delta\mathbf{v}^h$  as the output. The procedure proceeds until the residual is sufficiently small. By replacing the embedded Jacobi solver with Gauss-Seidel solver, we can similarly formulate the HINTS-GS.

Another more advanced option is to consider combining DeepONet with multigrid methods, yielding the HINTS-MG algorithm (see pseudo-code in Section S3 in SI). For a V-cycle multigrid algorithm (see Section S1 in SI), we replace a proportion of Jacobi/Gauss-Seidel relaxation at each grid level by the DeepONet solver. We anticipate that HINTS-MG will benefit from advantages of multigrid methods, hence providing even better performance compared to HINTS-Jacobi.

Notably, the DeepONet solver is flexible with regards to the domain discretization of the numerical problem. A DeepONet trained on discretization  $\Omega^{h_D}$  can be transferred to a numerical problem with another discretization  $\Omega^h$ , by simply including an interpolation step in the input side of DeepONet. This step enables a single HINTS to be used for solving equations equipped with different discretizations, involving different mesh densities, non-uniform meshes, and/or irregular meshes. For the HINTS-MG solver, in particular, this characteristic makes it possible to apply one single DeepONet for all levels of grids.

We employ HINTS for the following two prototypical equations:

- Poisson equation:

$$\nabla \cdot \left( k(\mathbf{x}) \nabla u(\mathbf{x}) \right) + f(\mathbf{x}) = 0, \quad \mathbf{x} \in \Omega \subset \mathbb{R}^d \quad (4a)$$

$$u(\mathbf{x}) = 0, \quad \mathbf{x} \in \partial\Omega; \quad (4b)$$

- Helmholtz equation:

$$\nabla^2 u(\mathbf{x}) + k^2(\mathbf{x})u(\mathbf{x}) = f(\mathbf{x}), \quad \mathbf{x} \in \Omega \subset \mathbb{R}^d \quad (5a)$$

$$u(\mathbf{x}) = 0, \quad \mathbf{x} \in \partial\Omega. \quad (5b)$$

The Helmholtz equation is indefinite for sufficiently large  $k(\mathbf{x})$ , making it hard to solve by many classical solvers. In the following subsections, we will examine the performance of HINTS by presenting a series of numerical examples for these two equations, including different spatial dimensions  $d$  ( $\in \{1, 2, 3\}$ ), different discretization methods (finite elements for the Poisson equation; finite differences for the Helmholtz equations), and different geometries. We mainly focus on HINTS-Jacobi, while presenting the study on HINTS-MG in the last subsection and HING-GS in Section S4 in SI, respectively.

## 2.2. Poisson Equation in One Dimension

As a first prototypical example, we consider the Poisson equation in one dimension ( $d = 1$ ), defined in  $\Omega = (0, 1)$ . The goal of HINTS-Jacobi is to solve this equation with arbitrary  $k(x)$  and  $f(x)$ . We first train a DeepONet with paired data  $[k(x), f(x)]$  (generated by a Gaussian random field) and corresponding  $u(x)$ . Details and results of training are included in Section S4 in SI. After training, we employ HINTS-Jacobi to solve for new instances of  $k(x)$  and  $f(x)$ . Here, we employ the same discretization for the DeepONet and the numerical problem ( $\Omega^{h_D} = \Omega^h$ ,  $n_D = n = 30$ ).

We show the performance of HINTS-Jacobi for a representative choice of  $(k(x), f(x))$  in Fig. 2. Results for other  $(k(x), f(x))$  and for HINTS-GS are presented in Section S4 in SI. Fig. 2A shows the profiles of  $k(x)$  and  $f(x)$  considered. In Fig. 2B, we show the profiles of typical eigenmodes  $\phi_i^h$  ( $\phi_i(x); i \in \{1, 5, 10\}$ ) of the solution  $u(x)$  and corresponding loading vectors  $(\frac{\mathbf{A}^h \phi_i^h}{\|\mathbf{A}^h \phi_i^h\|})$ , where mode 1 refers to the lowest-frequency mode and mode 10 is a mode with relatively high frequency. In Fig. 2C, we present the numerical results for three setups (see the first column): (Setup 1) Jacobi solver; (Setup 2) Jacobi solver initialized with a single DeepONet inference; (Setup 3) HINTS-Jacobi (with DeepONet

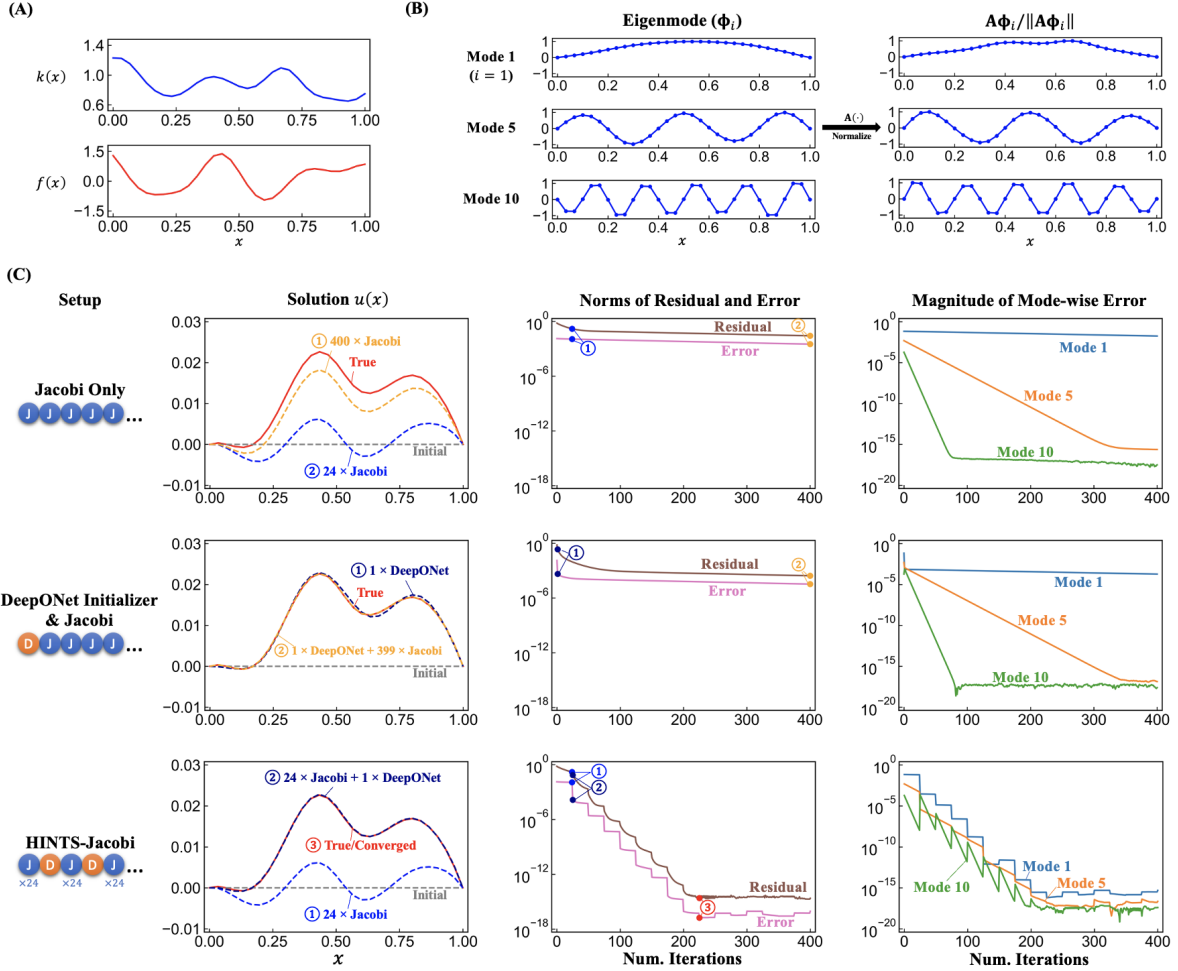


Figure 2: **Results of 1D Poisson Equation** ( $\frac{d}{dx}(k(x)\frac{d}{dx}u(x)) + f(x) = 0$ ). (A) Profiles of  $k(x)$  and  $f(x)$ . (B) Eigenmodes  $\phi_i^h$  ( $\phi_i(x)$ ;  $i = 1, 5, 10$  herein) and corresponding loading vectors  $\frac{\mathbf{A}^h \phi_i^h}{\|\mathbf{A}^h \phi_i^h\|}$  of the Jacobi solver. Mode 1 has the lowest spatial frequency, while mode 10 has a relatively high spatial frequency. (C) Numerical results. We consider three setups, each shown in one row: (Setup 1) Jacobi solver only; (Setup 2) Jacobi solver with DeepONet initializer, i.e., one-time usage of DeepONet followed by Jacobi iterations; (Setup 3) HINTS-Jacobi (with a DeepONet-to-Jacobi ratio 1 : 24). The second column shows key snapshots of the iterative solution. For a linear system  $\mathbf{A}^h \mathbf{u}^h = \mathbf{f}^h$  with approximate solution  $\mathbf{v}^h \approx \mathbf{u}^h$ , the residual is defined by  $\mathbf{r}^h := \mathbf{f}^h - \mathbf{A}^h \mathbf{v}^h$ . The third column shows the histories of the norms of residual and error of the approximate solution, with the snapshots in the second column marked correspondingly. The fourth column shows the history of the norm of error for eigenmodes 1, 5, and 10.



proportion  $1/25$ ). In the second and the third columns, we show key snapshots of the approximate solution and the norms of residual and error of the approximate solution, respectively, where the reference/true solution for comparison comes from direct inversion of the linear equations. After 400 iterations, the approximate solution of Setup 1 is still visually different from the true solution  $u(x)$ , with the absolute error being  $\mathcal{O}(10^{-2})$ . Setup 2 provides a better estimate, with an absolute error  $\mathcal{O}(10^{-4})$  that is substantially smaller than Setup 1. However, the contribution of the one-time DeepONet initialization in Setup 2 is marginal – it does not change the convergence rate, and the solution is still far from convergence to machine zero. On the contrary, Setup 3, i.e., HINTS-Jacobi, provides a solution that rapidly converges to machine zero ( $\mathcal{O}(10^{-16})$ ) within roughly 200 iterations.

In the last column of Fig. 2C, we display the history of the eigenmode-wise error for modes 1, 5, and 10. For all the setups, the convergence rate of the embedded Jacobi iterations is uniform for each mode, matching the theoretical analysis in Section S1 in SI. For Setups 1 and 2, the slow convergence of mode 1 in the Jacobi solver is the bottleneck of the overall convergence rate. The embedded DeepONet iterations, on the other hand, make a substantial difference in Setup 3. DeepONet iterations significantly reduce mode-1 error, hence breaking the bottleneck effect in restricting the overall convergence rate. While DeepONet iterations have limited improvements for mode 5 and even negative effects on mode 10, these two modes are well resolved by the Jacobi solver. With such an observation, we find that the mixture of the two solvers functions in a synergetic way: the Jacobi solver is efficient for high-frequency modes but not for low-frequency modes; the DeepONet solver provides fast approximate solutions for low frequencies but may pollute the high frequencies. A proper combination of these two methods synchronizes the convergence paths and enables fast and uniform convergence across all eigenmodes.

We present additional results for the 1D Poisson equation in Section S4 in SI, including those for (1) other  $k(x)$  and  $f(x)$ , (2) HINTS-GS and (3) different discretizations for

DeepONet and the numerical problem (i.e.,  $\Omega^{h_D} \neq \Omega^h$ , or  $n_D \neq n$ ). The performance of HINTS is consistent with the results in Fig. 2 for both cases, which demonstrates (1) effectiveness of HINTS in its integration with the Gauss-Seidel method, and (2) the transferability of HINTS across different domain discretizations.

### 2.3. Analyzing HINTS

From the mode-wise errors in Fig. 2C, we have shown that DeepONet performs well for the low-frequency modes in the solution. This characteristic is associated with the fact that the DeepONet training data are generated from a Gaussian random field with a certain correlation length, which mainly contains frequencies within a certain range. Previous studies on DeepONet have found that DeepONet generalizes well towards frequencies lower than the training data but not for higher frequencies [41, 46]. Hence, we expect that the trained DeepONet can predict well solutions of mode 1, 2, ...,  $n_{\text{cut}}$ , where  $n_{\text{cut}}$  is a cutoff frequency. To further demonstrate this, we examine the mode-wise performance of DeepONet in Fig. 3A. Row  $j$  ( $j \in \{1, 2, \dots, 15\}$ ) represents the test of DeepONet with the input  $f(x)$  corresponding to  $u(x) = \phi_j(x)$ , i.e., the solution with eigenmode  $j$  only. The mode-wise errors of the DeepONet prediction/output are shown in different columns. The displayed error values are the geometric mean of 100 test cases of  $k(x)$ . We note that  $n_{\text{cut}} = 7$  for the current setup. For tests on the first seven modes (rows 1 to 7), DeepONet uniformly decreases errors in all modes. For tests starting from the eighth mode, DeepONet is unable to decrease the error of the input mode (shown in diagonal blocks), and even produces errors in modes 1 to 7. We point out that this  $n_{\text{cut}}$  relies on the performance of DeepONet, which is influenced by diverse factors in its training process, such as size and correlation length of training data. We include a systematic study on these factors in Section S4 in SI.

We found that a mixture of solvers helps accelerates the solution. A natural question is: what is the optimal proportion of DeepONet in HINTS? Intuitively, based on the preceding analysis, too large a proportion of DeepONet does not allow the Jacobi solver

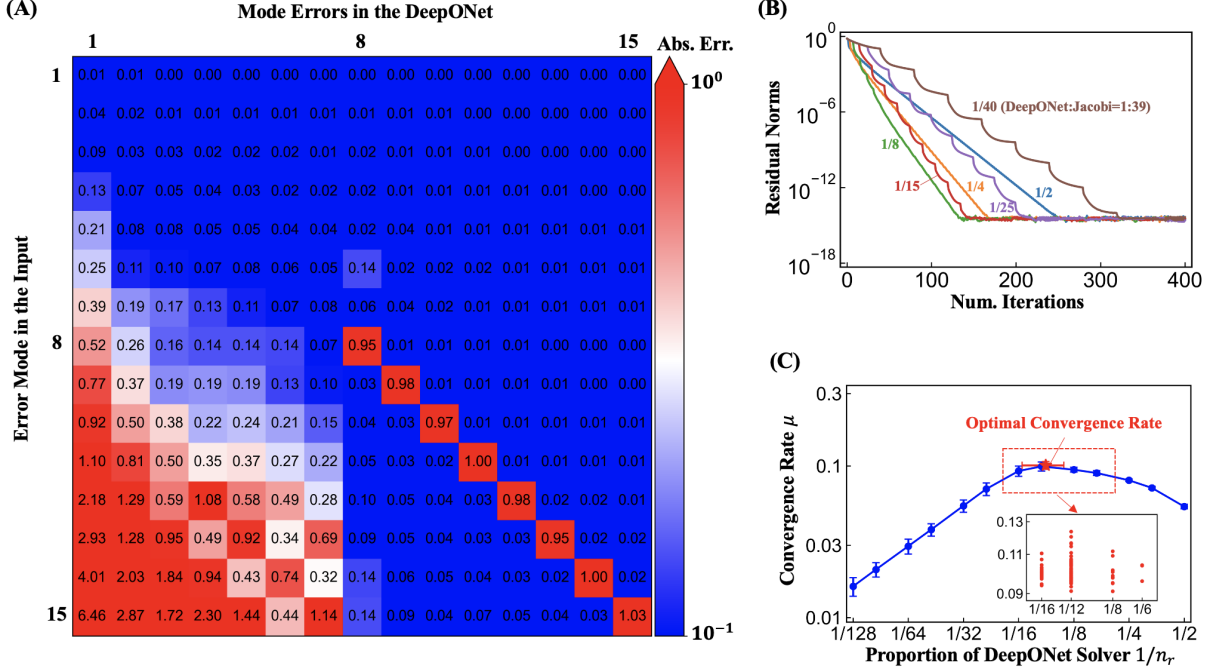


Figure 3: **Analysis of HINTS-Jacobi for 1D Poisson Equation.** (A) Mode-wise performance of the trained DeepONet. Row  $j$  ( $j \in \{1, 2, \dots, 15\}$ ) represents the test of DeepONet with input  $f(x)$  corresponding to true solution  $u(x) = \phi_j(x)$ , i.e., only the eigenmode  $j$ . The mode-wise errors of the DeepONet prediction/output are shown in different columns. (B) Convergence histories of residual norms for different proportions of DeepONet in HINTS-Jacobi. Shown are the results for the test case  $(k(x), f(x))$  in Fig. 2A. For a linear system  $\mathbf{A}^h \mathbf{u}^h = \mathbf{f}^h$  with approximate solution  $\mathbf{v}^h \approx \mathbf{u}^h$ , the residual is defined by  $\mathbf{r}^h := \mathbf{f}^h - \mathbf{A}^h \mathbf{v}^h$ . (C) Convergence rates  $\mu$  for different proportions of DeepONet ( $1/n_r$ ) in HINTS-Jacobi. We show the mean value and standard deviation of  $\mu$  for 100 test cases in blue. The mean and standard deviation of the optimal convergence rate is marked by red. In the inset, we show the locations corresponding to the optimal convergence rate for all test cases.

to cause a sufficient decay of high-frequency errors, so that the DeepONet receives inputs contaminated by high-frequency modes beyond its cutoff frequency. On the other hand, a too small proportion of DeepONet causes excessive Jacobi iterations that suffer from slow convergence for low-frequency modes. In Fig. 3B, we show the residual norms for six different proportions of DeepONet, ranging from  $1/40$  to  $1/2$ , for the test case in Fig. 2A. We observe non-monotonic convergence rates of convergence with respect to DeepONet

proportions. To better quantify this, we define the convergence rate  $\mu$  of an iterative solver by

$$\mu := -\frac{1}{k_{\text{it,start}} - k_{\text{it,end}}} \log_{10} \frac{\|\mathbf{r}^{h(k_{\text{it,end}})}\|}{\|\mathbf{r}^{h(k_{\text{it,start}})}\|}, \quad (6)$$

where  $k_{\text{it,start}}$  and  $k_{\text{it,end}}$  are two snapshots between which the residual decays steadily. Intuitively, this convergence rate  $\mu$  represents how many orders of magnitude of the residual are decayed in each iteration, which is proportional to the slopes of lines in figures such as Fig. 3B. We show the statistics of  $\mu$  for different DeepONet proportions  $1/n_r$  for all 100 test cases in Fig. 3C. In this particular setup, the optimal proportions range from  $1/16$  to  $1/6$ , with the mean value being approximately  $1/12$ . In Section S4 in SI, we include additional studies on factors influencing this optimal proportion.

#### 2.4. Solving Equations Involving Indefiniteness

In the preceding example of the Poisson equation, the linear system is positive definite, which can be solved by all classical numerical solvers. Here, we consider the 1D Helmholtz equation (Eq. 5) in  $\Omega = (0, 1)$ , where the indefiniteness results in divergence of many classical solvers. After the offline training of a DeepONet on 1D Helmholtz data, we use the HINTS-Jacobi algorithm to solve for new instances  $k(x)$  and  $f(x)$  with the same discretization  $n = n_D = 30$ . We display the results in Fig. 4 in a similar way to Fig. 2 for the Poisson equation. As analyzed in Section S1 in SI, the first two setups diverge due to the divergence of low-frequency modes for indefinite systems. Setup 3, i.e., the HINTS-Jacobi (with DeepONet proportion  $1/15$ ), is capable of reaching convergence to machine zero after roughly 300 iterations. Here, HINTS-Jacobi functions in a similar but not identical way as for Poisson equation – the DeepONet solver decreases the error of low-frequency modes, counteracting the Jacobi solver that slowly increases the error, while leaving high-frequency modes to be handled by the Jacobi solver. The HINTS-Jacobi resolves the issue of divergence for indefinite systems, which is prevalent for classical numerical solvers.

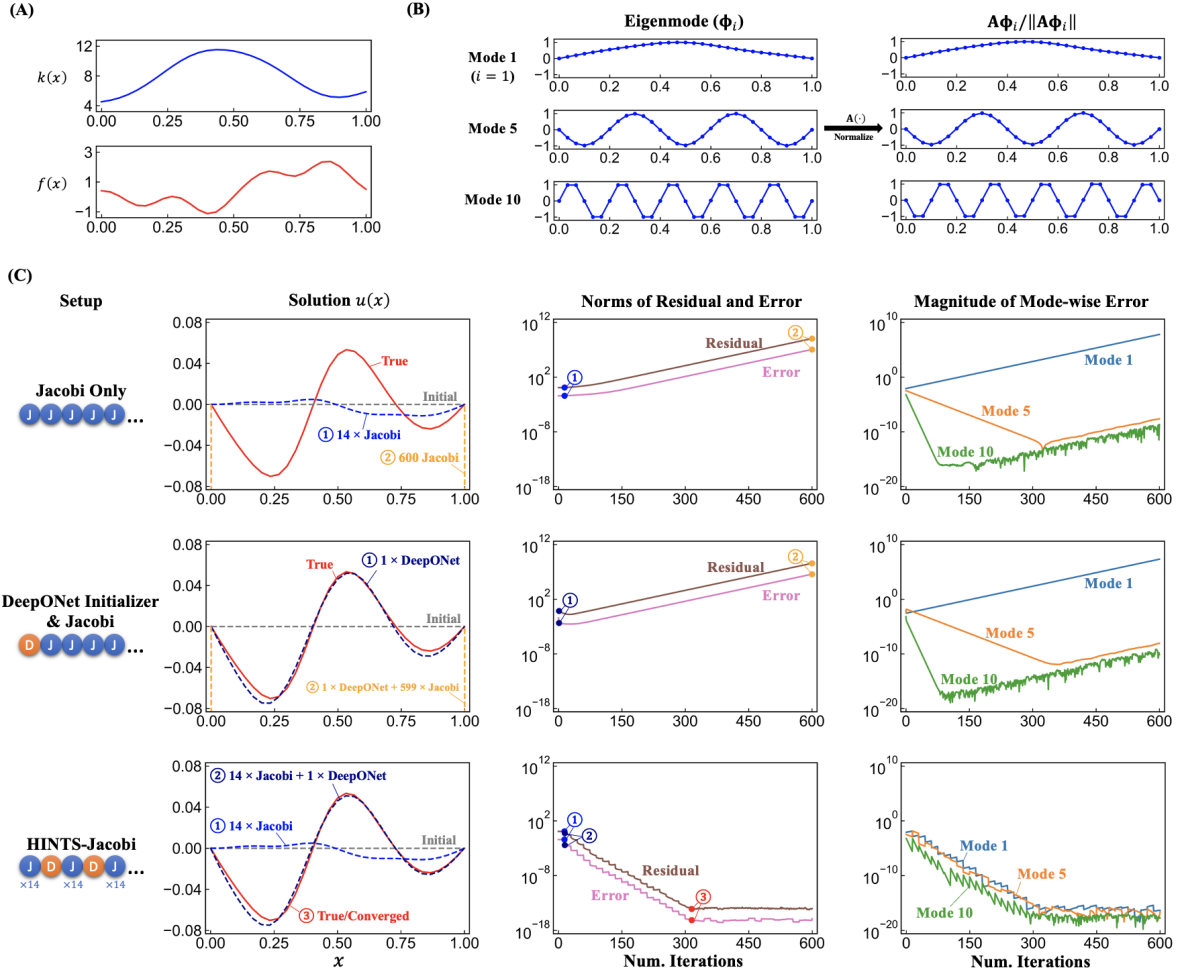


Figure 4: **Results of 1D Helmholtz Equation** ( $\frac{d^2}{dx^2}u(x) + k^2(x)u(x) = f(x)$ ). (A) Profiles of  $k(x)$  and  $f(x)$ . (B) Eigenmodes  $\phi_i^h$  ( $\phi_i(x)$ ;  $i = 1, 5, 10$  herein) and corresponding loading vectors  $\frac{\mathbf{A}^h \phi_i^h}{\|\mathbf{A}^h \phi_i^h\|}$  of the Jacobi solver. Mode 1 has the lowest spatial frequency, while mode 10 has a relatively high spatial frequency. (C) Numerical results. We consider three setups, each shown in one row: (Setup 1) Jacobi solver only; (Setup 2) Jacobi solver with DeepONet initializer, i.e., one-time usage of DeepONet followed by Jacobi iterations; (Setup 3) HINTS-Jacobi (with a DeepONet-to-Jacobi ratio 1 : 14). The second column shows key snapshots of the iterative solution. For a linear system  $\mathbf{A}^h \mathbf{u}^h = \mathbf{f}^h$  with approximate solution  $\mathbf{v}^h \approx \mathbf{u}^h$ , the residual is defined by  $\mathbf{r}^h := \mathbf{f}^h - \mathbf{A}^h \mathbf{v}^h$ . The third column shows the histories of the norms of residual and error of the approximate solution, with the snapshots in the second column marked correspondingly. The fourth column shows the history of the norm of error in eigenmodes 1, 5, and 10.

### 2.5. Multidimensions and Irregular Geometries

The effectiveness of HINTS is not limited to one-dimensional problems equipped with uniform grids. Next, we consider equations in multidimensions ( $d \geq 2$ ). Due to the discretization transferability, HINTS is capable of adapting to an irregular computational domain (e.g., triangular  $\Omega$ ) and/or irregular discretizations (e.g.,  $\Omega^h$  with triangular elements). Here, we consider the following multi-dimensional examples with HINTS-Jacobi:

- 2D Poisson equation defined in an L-shaped domain:  $\Omega := (0, 1)^2 \setminus [0.5, 1)^2$ ;
- 3D Helmholtz equation defined in an unit square:  $\Omega := (0, 1)^3$ .

We illustrate the geometries in the first column of the first rows in Fig. 5A (2D Poisson) and Fig. 5B (3D Helmholtz). In particular, the case of 2D Poisson equation uses finite element discretization with linear triangular meshes ( $\Omega^h$ ), while we still use a DeepONet trained on a uniform mesh ( $\Omega^{h_D}$ ). Both cases adopt the DeepONet proportion 1/15 (see more details in Section S3 in SI). The remaining results in the first rows of Figs. 5A-B, similar to 1D cases, show the histories of the norms of the residual, error, and the mode-wise error. The second rows show the error of three key snapshots (marked in the residual/error history) during the iterations together with the true/converged solution. For the case of 3D Helmholtz equation, we display the cross section at  $z = 0.5$ . In both cases, DeepONet iterations significantly reduce the errors or low-frequency modes, hence accelerating the convergence of the solution. In Section S4 in SI, we present the results of the 3D Helmholtz equation solved with HINTS-GS and the results of a 2D Helmholtz equation defined in  $\Omega := (0, 1)^2$ .

### 2.6. Integrating HINTS with Multigrid Methods

Finally, we focus on HINTS-MG, the hybrid solver that integrates DeepONet with multigrid methods. We apply HINTS-MG to solve the 1D Poisson equation (Eq. 4;  $\Omega = (0, 1)$ ) and the 2D Helmholtz equation (Eq. 5;  $\Omega = (0, 1)^2$ ), with the results shown in Fig. 6A and Fig. 6B, respectively. For the 1D Poisson equation, we consider the same

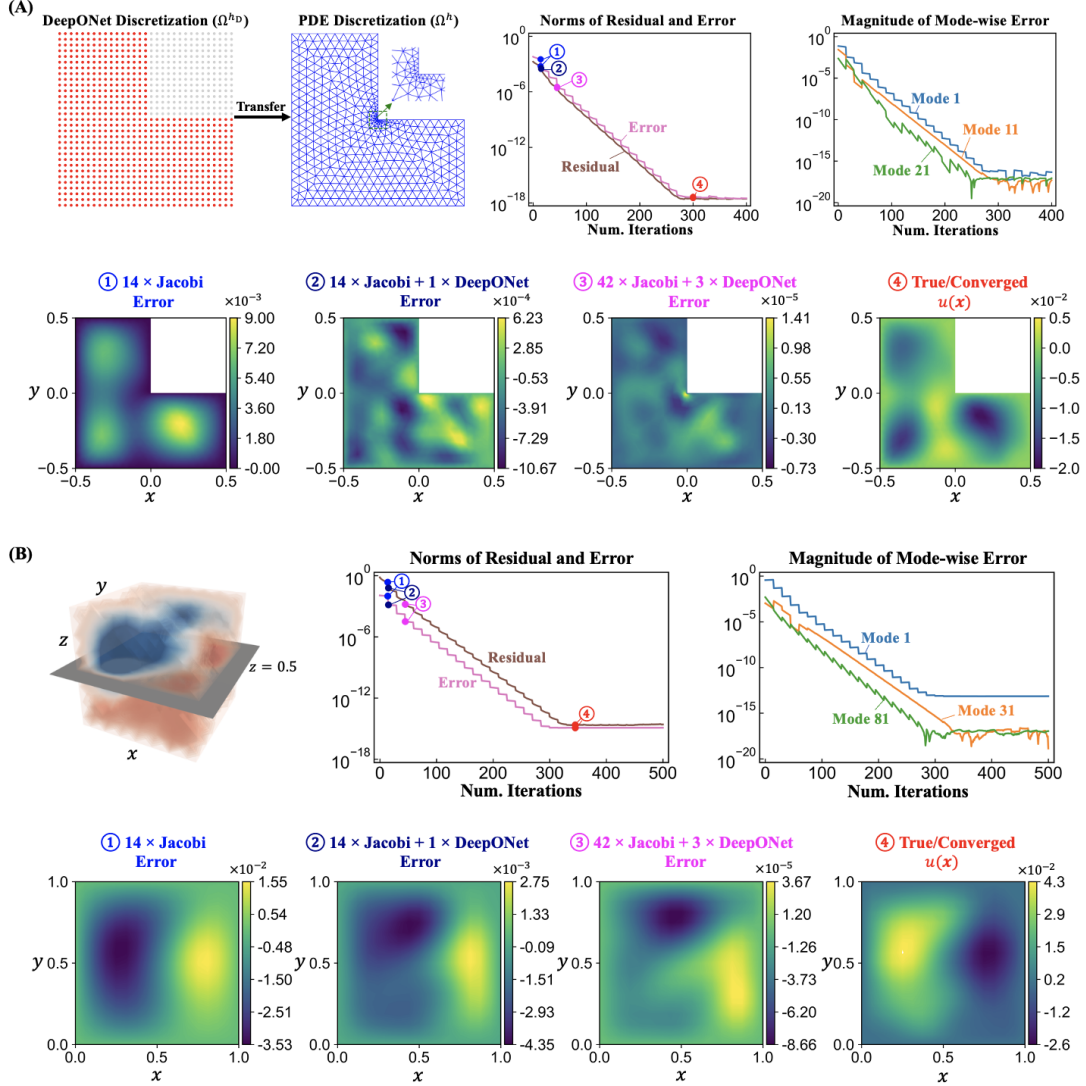


Figure 5: **Results of HINTS-Jacobi for 2D Poisson Equation and 3D Helmholtz Equation.** The DeepONet-to-Jacobi ratio is 1 : 14 in both cases. (A) 2D Poisson equation. In the first row, the first and the second columns shows the discretization of DeepONet and the numerical problem, respectively; the third and the fourth columns show the histories of norms of errors and residuals and mode-wise errors, respectively. In the second row, we display the profiles of errors of some key snapshots together with the true/converged solution. (B) 3D Helmholtz equation. In the first row, the first column illustrates the 3D domain where we define the problem. Other displays are similar to Poisson equation in (A). The snapshots show the errors and true solution on cross section  $z = 0.5$ , marked in the first panel.

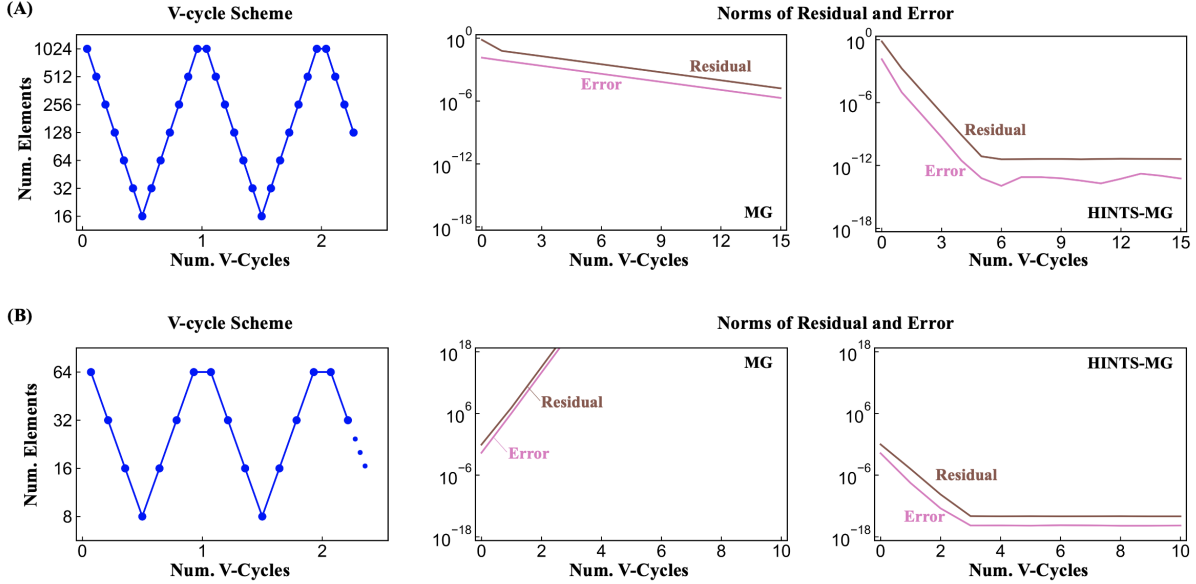


Figure 6: **Results of HINTS-MG for 1D Poisson Equation and 2D Helmholtz Equation.** (A) 1D Poisson Equation. The first column shows the setup of V-cycle in the multigrid algorithm, where each dot represents 10 iterations. The second and the third column compare the histories of norms of errors and residuals for the two setups of relaxation: (Setup M1) with Gauss-Seidel relaxation only; (Setup M2) with hybrid DeepONet-GS relaxation (1 : 9 in each grid level). (B) 2D Helmholtz equation. Display is similar to (A). The DeepONet-GS ratio is also 1 : 9.

$k(x)$  and  $f(x)$  as shown in Fig. 2A. We discretize the domain into  $n = 1024$  uniform intervals, and adopt the V-cycle scheme with 7 levels to solve the system (see Fig. 6A). We consider two setups for relaxation: (Setup M1) Gauss-Seidel relaxation only; (Setup M2) HINTS-MG with DeepONet-GS relaxation (DeepONet proportion 1/10). We present the histories of the norms of residual and error (second column) and the mode-wise error (third column) against the number of V-cycles in Fig. 6A. By introducing DeepONet, the number of V-cycles needed for achieving machine zero is significantly decreased to roughly 5. For the 2D Helmholtz equation, we show the results for  $n = 64^2$  and four grid levels in Fig. 6B. While the classical multigrid solver diverges, HINTS-MG converges to machine zero within approximately 3 V-cycles. Through the results presented in Fig. 6, we demonstrated the potential of HINTS in combining with advanced numerical solvers,



for further improving the computational efficiency and range of applicability.

### 3. Discussion

We have demonstrated the capability of HINTS in solving linear differential equations. HINTS is fast, accurate, and widely applicable to diverse classes of differential equations. The method is agnostic in terms of the differential equations, computational domains (shape and dimension), and discretization. More importantly, HINTS can be transferred to discretizations that are different from the discretization based on which it is trained.

We conducted a systematic study on the performance of HINTS-Jacobi, where we examined why and how this hybrid solver functions. In summary, the embedded DeepONet solver provides fast, approximate solutions for low-frequency eigenmodes in the solution, while the embedded Jacobi solver handles the remaining higher-frequency eigenmodes, guaranteeing the convergence of the solver. Such a combination of solvers incorporates advantages from both ends, improving the performance beyond individual solvers: classical solvers either are slow or even fail to convergence; an individual deep learning solver may only provide an approximate solution. We emphasize that to introduce deep learning into numerical solvers, integration works better than substitution. A hybrid methodology, instead of starting from scratch, retains the advantages from numerical solvers that have been studied for centuries. While the DeepONet is trained with a finite dataset, the setup of HINTS enables the generalization into infinite test cases with the preservation of convergence to machine zero.

When training a deep neural network, one frequently observes a phenomenon called spectral bias [77]. This refers to the fact that neural networks tend to learn the lower part of the spectrum first. The vast majority of applications of neural networks suffer from such a spectral bias, which inhibits the networks from learning complex mappings. On the contrary, interestingly, HINTS exploits such a bias to tackle low-frequency modes that are otherwise difficult for classical solvers which, essentially, are biased towards high

frequencies. By replacing the classical solver with the DeepONet solver for a limited proportion of iterations, HINTS balances the convergence rates across the spectrum of eigenmodes, significantly improving the computational efficiency and simplifying tremendously implementation and software.

In the foregoing Results section, we present the computational efficiency with respect to the number of iterations, which is meaningful as we analyze the characteristic of HINTS as a numerical method. Practically, on the other hand, one cares more about the wall-clock time cost of an algorithm. In Section S4 in SI, we present additional results comparing the time cost of the Jacobi method, the multigrid method, HINTS-Jacobi, and HINTS-MG for 1D Poisson equation with various numbers of elements  $n$ . The results show that HINTS performs consistently better than the corresponding numerical methods, with the improvement of computational efficiency being up to  $\mathcal{O}(10^2)$ .

HINTS is promising in practical applications in many fields of real-world science and engineering. One may build HINTS based on existing numerical solvers, by adding a simple conditional statement to integrate DeepONet in a plug-and-play style. Moreover, since DeepONet fits into the regular solver routine, HINTS is fully parallelizable, e.g., it is embarrassingly parallel for the Jacobi version. Such parallelizability endows HINTS with unique advantages in multidimensional, large-scale systems with practical interest.

HINTS represent a general class of methodology where one integrates operator regressors with standard numerical solvers. While we have systematically studied several instances, future works are still needed for further investigation of this hybrid methodology. First, one may investigate other solvers to be integrated on both sides. Second, while we focus on the classes of differential equations parameterized by  $k(\mathbf{x})$  and  $f(\mathbf{x})$  within the equations, other forms of parameterization, such as geometric domain, boundary conditions, etc., are needed for adapting to different problems of interest. Third, a similar methodology may be extended to nonlinear problems, which are of more practical importance and are more difficult to solve.

## 4. Methods

### 4.1. Numerical Solvers

In the study related to the Jacobi solver, we use the damped Jacobi method, with a damping parameter  $\omega = 2/3$  for one-dimensional cases,  $\omega = 4/5$  for two-dimensional cases,  $\omega = 6/7$  for three-dimensional cases. These choices are shown to be optimal for Poisson equation [27]. In the study related to multigrid methods, we consider V-cycles with Gauss-Seidel relaxation. We conduct Gauss-Seidel relaxation in each grid level (including both the finest and coarsest levels). We implemented the full-weighting version of the restrictor and the prolongator. Additional technical details are summarized in Section S3 in SI.

### 4.2. DeepONet

We use the standard architecture of DeepONet [35] in this study.  $k(\mathbf{x})$  (similarly for  $f(\mathbf{x})$ ) is fed into the branch network in the discrete form  $[k(\mathbf{x}_0), k(\mathbf{x}_1), \dots, k(\mathbf{x}_{n_D})]^T$ , where  $\{\mathbf{x}_i\}_{i=0}^{n_D}$  are uniform grid points in  $\Omega$ . Then, for an arbitrary  $\mathbf{x} \in \Omega$ , which is received at the trunk network, DeepONet predicts  $u(\mathbf{x})$  that approximately satisfies Eq. 1. The branch network is a dense neural network for problems in 1D and a convolutional neural network for problems in multidimensions. We enforce the Dirichlet boundary conditions by postprocessing DeepONet outputs for all cases except the 2D Poisson equation in an L-shaped domain. Specifically, for problems defined in  $\Omega = (0, 1)^d$  ( $d \in \{1, 2, 3\}$ ), the original output of the DeepONet is multiplied by  $x(x - 1)$ ,  $xy(x - 1)(y - 1)$ ,  $xyz(x - 1)(y - 1)(z - 1)$  for  $d = 1, 2, 3$ , respectively. To ensure convergence to machine zero, we utilize the scaling of  $f(x)$  in the DeepONet. Before feeding into the DeepONet,  $f(x)$  is normalized. Then, the norm is multiplied to the output of the DeepONet. Additional technical details are summarized in Section S3 in SI.

### 4.3. HINTS

The pseudocode related to HINTS is given in Section S3 in SI. Note that DeepONet predicts the correction of the solution corresponding to the current residual (see Eq. 3).

To solve a single differential equation with a specified  $k(\mathbf{x})$  and  $f(\mathbf{x})$ , DeepONet iterations take the same  $k(\mathbf{x})$  as the first input in Eq. 2 but different right-hand-side forcing terms  $r(\mathbf{x})$  corresponding to the current residual in the iterative process as the second input. Before invoking the DeepONet solver, we need the reversion of the matrix- (vector-) form residual  $\mathbf{r}^h$  into the function-form residual  $r(\mathbf{x})$ . In addition, for numerical examples involving different discretizations of DeepONet and the numerical problem (i.e.,  $\Omega^h \neq \Omega^{h_D}$ ), we need to interpolate  $\Omega^h$  into  $\Omega^{h_D}$  before feeding the data into DeepONet. No additional steps are needed on the output side, since DeepONet is capable of evaluating the output function for  $\Omega^h$ . Additional technical details are summarized in Section S3 in SI.

## References

- [1] S. C. Chapra, R. P. Canale, et al., Numerical methods for engineers, volume 1221, Mcgraw-hill New York, 2011.
- [2] J. H. Mathews, Numerical methods for mathematics, science and engineering, volume 10, Prentice-Hall International, 1992.
- [3] P. Bodenheimer, Numerical methods in astrophysics: an introduction, CRC Press, 2006.
- [4] M. Feit, J. Fleck Jr, A. Steiger, Solution of the schrödinger equation by a spectral method, Journal of Computational Physics 47 (1982) 412–433.
- [5] A. T. Patera, A spectral element method for fluid dynamics: laminar flow in a channel expansion, Journal of Computational Physics 54 (1984) 468–488.
- [6] J. Kim, P. Moin, R. Moser, Turbulence statistics in fully developed channel flow at low reynolds number, Journal of Fluid Mechanics 177 (1987) 133–166.

- [7] B. Cockburn, G. E. Karniadakis, C.-W. Shu, Discontinuous Galerkin methods: theory, computation and applications, volume 11, Springer Science & Business Media, 2012.
- [8] T. J. Hughes, The finite element method: linear static and dynamic finite element analysis, Courier Corporation, 2012.
- [9] J. C. Simo, T. J. Hughes, Computational inelasticity, volume 7, Springer Science & Business Media, 2006.
- [10] T. J. Hughes, J. A. Cottrell, Y. Bazilevs, Isogeometric analysis: Cad, finite elements, nurbs, exact geometry and mesh refinement, Computer Methods in Applied Mechanics and Engineering 194 (2005) 4135–4195.
- [11] L. Jing, J. Hudson, Numerical methods in rock mechanics, International Journal of Rock Mechanics and Mining Sciences 39 (2002) 409–427.
- [12] M. Rappaz, M. Bellet, M. O. Deville, R. Snyder, Numerical modeling in materials science and engineering, Springer, 2003.
- [13] J. A. Kong, L. Tsang, K.-H. Ding, C. O. Ao, Scattering of electromagnetic waves: numerical simulations, John Wiley & Sons, 2004.
- [14] J. C. Strikwerda, Finite difference schemes and partial differential equations, SIAM, 2004.
- [15] K.-J. Bathe, Finite element procedures, Klaus-Jurgen Bathe, 2006.
- [16] G. E. Karniadakis, G. Karniadakis, S. Sherwin, Spectral/hp element methods for computational fluid dynamics, Oxford University Press on Demand, 2005.
- [17] R. L. Burden, J. D. Faires, A. M. Burden, Numerical analysis, Cengage learning, 2015.

- [18] H. A. Van der Vorst, *Iterative Krylov methods for large linear systems*, 13, Cambridge University Press, 2003.
- [19] T. Mathew, *Domain decomposition methods for the numerical solution of partial differential equations*, volume 61, Springer Science & Business Media, 2008.
- [20] J. Xu, *Iterative methods by space decomposition and subspace correction*, *SIAM Review* 34 (1992) 581–613. doi:10.1137/1034116.
- [21] A. Greenbaum, *Iterative methods for solving linear systems*, SIAM, 1997.
- [22] M. A. Olshanskii, E. E. Tyrtshnikov, *Iterative methods for linear systems: theory and applications*, SIAM, 2014.
- [23] Y. Saad, *Iterative methods for sparse linear systems*, SIAM, 2003.
- [24] D. A. Knoll, D. E. Keyes, *Jacobian-free newton–krylov methods: a survey of approaches and applications*, *Journal of Computational Physics* 193 (2004) 357–397.
- [25] G. Ciaramella, M. J. Gander, *Iterative methods and preconditioners for systems of linear equations*, SIAM, 2022.
- [26] M. J. Gander, T. Lunet, D. Ruprecht, R. Speck, *A unified analysis framework for iterative parallel-in-time algorithms*, *arXiv preprint arXiv:2203.16069* (2022).
- [27] W. L. Briggs, V. E. Henson, S. F. McCormick, *A multigrid tutorial*, SIAM, 2000.
- [28] W. Hackbusch, *Multi-grid methods and applications*, volume 4, Springer Science & Business Media, 2013.
- [29] J. H. Bramble, *Multigrid methods*, Chapman and Hall/CRC, 2019.
- [30] Y. Shapira, *Matrix-based multigrid: theory and applications*, Springer, 2008.

- [31] A. AlOnazi, G. S. Markomanolis, D. Keyes, Asynchronous task-based parallelization of algebraic multigrid, in: Proceedings of the Platform for Advanced Scientific Computing Conference, 2017, pp. 1–11.
- [32] L. Berger-Vergiat, H. Waisman, B. Hiriyur, R. Tuminaro, D. Keyes, Inexact schwarz-algebraic multigrid preconditioners for crack problems modeled by extended finite element methods, *International Journal for Numerical Methods in Engineering* 90 (2012) 311–328.
- [33] B. Hiriyur, R. S. Tuminaro, H. Waisman, E. G. Boman, D. Keyes, A quasi-algebraic multigrid approach to fracture problems based on extended finite elements, *SIAM Journal on Scientific Computing* 34 (2012) A603–A626.
- [34] J. H. Bramble, J. E. Pasciak, J. Xu, Parallel multilevel preconditioners, *Mathematics of Computation* 55 (1990) 1–22.
- [35] L. Lu, P. Jin, G. Pang, Z. Zhang, G. E. Karniadakis, Learning nonlinear operators via deepnet based on the universal approximation theorem of operators, *Nature Machine Intelligence* 3 (2021) 218–229.
- [36] Z. Li, N. Kovachki, K. Azizzadenesheli, B. Liu, K. Bhattacharya, A. Stuart, A. Anandkumar, Fourier neural operator for parametric partial differential equations, *arXiv preprint arXiv:2010.08895* (2020).
- [37] G. Kissas, J. Seidman, L. F. Guilhoto, V. M. Preciado, G. J. Pappas, P. Perdikaris, Learning operators with coupled attention, *arXiv preprint arXiv:2201.01032* (2022).
- [38] R. G. Patel, N. A. Trask, M. A. Wood, E. C. Cyr, A physics-informed operator regression framework for extracting data-driven continuum models, *Computer Methods in Applied Mechanics and Engineering* 373 (2021) 113500.

- [39] T. Chen, H. Chen, Universal approximation to nonlinear operators by neural networks with arbitrary activation functions and its application to dynamical systems, *IEEE Transactions on Neural Networks* 6 (1995) 911–917.
- [40] L. Lu, X. Meng, S. Cai, Z. Mao, S. Goswami, Z. Zhang, G. E. Karniadakis, A comprehensive and fair comparison of two neural operators (with practical extensions) based on fair data, *Computer Methods in Applied Mechanics and Engineering* 393 (2022) 114778.
- [41] C. Lin, Z. Li, L. Lu, S. Cai, M. Maxey, G. E. Karniadakis, Operator learning for predicting multiscale bubble growth dynamics, *The Journal of Chemical Physics* 154 (2021) 104118.
- [42] S. Cai, Z. Wang, L. Lu, T. A. Zaki, G. E. Karniadakis, Deepm&mnet: Inferring the electroconvection multiphysics fields based on operator approximation by neural networks, *Journal of Computational Physics* 436 (2021) 110296.
- [43] P. C. Di Leoni, L. Lu, C. Meneveau, G. Karniadakis, T. A. Zaki, Deeponet prediction of linear instability waves in high-speed boundary layers, *arXiv preprint arXiv:2105.08697* (2021).
- [44] S. Goswami, M. Yin, Y. Yu, G. E. Karniadakis, A physics-informed variational deeponet for predicting crack path in quasi-brittle materials, *Computer Methods in Applied Mechanics and Engineering* 391 (2022) 114587.
- [45] M. Yin, E. Ban, B. V. Rego, E. Zhang, C. Cavinato, J. D. Humphrey, G. Em Karniadakis, Simulating progressive intramural damage leading to aortic dissection using deeponet: an operator–regression neural network, *Journal of the Royal Society Interface* 19 (2022) 20210670.
- [46] M. Yin, E. Zhang, Y. Yu, G. E. Karniadakis, Interfacing finite elements with deep



- neural operators for fast multiscale modeling of mechanics problems, *Computer Methods in Applied Mechanics and Engineering* (2022) 115027.
- [47] V. Oommen, K. Shukla, S. Goswami, R. Dingreville, G. E. Karniadakis, Learning two-phase microstructure evolution using neural operators and autoencoder architectures, *arXiv preprint arXiv:2204.07230* (2022).
- [48] S. Goswami, K. Kontolati, M. D. Shields, G. E. Karniadakis, Deep transfer learning for partial differential equations under conditional shift with deeponet, *arXiv preprint arXiv:2204.09810* (2022).
- [49] E. Zhang, B. Spronck, J. D. Humphrey, G. E. Karniadakis, G2 $\Phi$ net: Relating genotype and biomechanical phenotype of tissues with deep learning, *arXiv preprint arXiv:2208.09889* (2022).
- [50] M. Raissi, P. Perdikaris, G. E. Karniadakis, Physics-informed neural networks: A deep learning framework for solving forward and inverse problems involving nonlinear partial differential equations, *Journal of Computational physics* 378 (2019) 686–707.
- [51] M. Raissi, A. Yazdani, G. E. Karniadakis, Hidden fluid mechanics: Learning velocity and pressure fields from flow visualizations, *Science* 367 (2020) 1026–1030.
- [52] S. Cai, Z. Mao, Z. Wang, M. Yin, G. E. Karniadakis, Physics-informed neural networks (pinns) for fluid mechanics: A review, *Acta Mechanica Sinica* (2022) 1–12.
- [53] E. Zhang, M. Dao, G. E. Karniadakis, S. Suresh, Analyses of internal structures and defects in materials using physics-informed neural networks, *Science Advances* 8 (2022) eabk0644.
- [54] E. Zhang, M. Yin, G. E. Karniadakis, Physics-informed neural networks for nonhomogeneous material identification in elasticity imaging, *arXiv preprint arXiv:2009.04525* (2020).

- [55] M. Daneker, Z. Zhang, G. E. Karniadakis, L. Lu, Systems biology: Identifiability analysis and parameter identification via systems-biology informed neural networks, arXiv preprint arXiv:2202.01723 (2022).
- [56] Y. Chen, L. Lu, G. E. Karniadakis, L. Dal Negro, Physics-informed neural networks for inverse problems in nano-optics and metamaterials, *Optics Express* 28 (2020) 11618–11633.
- [57] S. Wang, H. Wang, P. Perdikaris, Learning the solution operator of parametric partial differential equations with physics-informed deepnets, *Science Advances* 7 (2021) eabi8605.
- [58] J. Sirignano, K. Spiliopoulos, Dgm: A deep learning algorithm for solving partial differential equations, *Journal of Computational Physics* 375 (2018) 1339–1364.
- [59] T. Pfaff, M. Fortunato, A. Sanchez-Gonzalez, P. W. Battaglia, Learning mesh-based simulation with graph networks, arXiv preprint arXiv:2010.03409 (2020).
- [60] T. Xue, A. Beatson, S. Adriaenssens, R. Adams, Amortized finite element analysis for fast pde-constrained optimization, in: *International Conference on Machine Learning*, PMLR, 2020, pp. 10638–10647.
- [61] D. Kochkov, J. A. Smith, A. Alieva, Q. Wang, M. P. Brenner, S. Hoyer, Machine learning-accelerated computational fluid dynamics, *Proceedings of the National Academy of Sciences* 118 (2021) e2101784118.
- [62] Z. Long, Y. Lu, X. Ma, B. Dong, Pde-net: Learning pdes from data, in: *International Conference on Machine Learning*, PMLR, 2018, pp. 3208–3216.
- [63] A. Kahana, E. Turkel, S. Dekel, D. Givoli, Obstacle segmentation based on the wave equation and deep learning, *Journal of Computational Physics* 413 (2020) 109458.

- [64] O. Ovadia, A. Kahana, E. Turkel, S. Dekel, Beyond the courant-friedrichs-lewy condition: Numerical methods for the wave problem using deep learning, *Journal of Computational Physics* 442 (2021) 110493.
- [65] J. Tompson, K. Schlachter, P. Sprechmann, K. Perlin, Accelerating eulerian fluid simulation with convolutional networks, in: *International Conference on Machine Learning*, PMLR, 2017, pp. 3424–3433.
- [66] K. Um, R. Brand, Y. R. Fei, P. Holl, N. Thuerey, Solver-in-the-loop: Learning from differentiable physics to interact with iterative pde-solvers, *Advances in Neural Information Processing Systems* 33 (2020) 6111–6122.
- [67] J.-T. Hsieh, S. Zhao, S. Eismann, L. Mirabella, S. Ermon, Learning neural pde solvers with convergence guarantees, *arXiv preprint arXiv:1906.01200* (2019).
- [68] J. He, J. Xu, Mgnet: a unified framework of multigrid and convolutional neural network, *Science China Mathematics* 62 (2019) 1331–1354.
- [69] Y. Chen, B. Dong, J. Xu, Meta-mgnet: Meta multigrid networks for solving parameterized partial differential equations, *Journal of Computational Physics* 455 (2022) 110996.
- [70] J. Huang, H. Wang, H. Yang, Int-deep: A deep learning initialized iterative method for nonlinear problems, *Journal of Computational Physics* 419 (2020) 109675.
- [71] Z. Zhang, Y. Wang, P. K. Jimack, H. Wang, Meshingnet: A new mesh generation method based on deep learning, in: *International Conference on Computational Science*, Springer, 2020, pp. 186–198.
- [72] H. Kato, Y. Ushiku, T. Harada, Neural 3d mesh renderer, in: *Proceedings of the IEEE conference on computer vision and pattern recognition*, 2018, pp. 3907–3916.

- [73] Y. Bar-Sinai, S. Hoyer, J. Hickey, M. P. Brenner, Learning data-driven discretizations for partial differential equations, *Proceedings of the National Academy of Sciences* 116 (2019) 15344–15349.
- [74] I. Luz, M. Galun, H. Maron, R. Basri, I. Yavneh, Learning algebraic multigrid using graph neural networks, in: *International Conference on Machine Learning*, PMLR, 2020, pp. 6489–6499.
- [75] D. Greenfeld, M. Galun, R. Basri, I. Yavneh, R. Kimmel, Learning to optimize multigrid pde solvers, in: *International Conference on Machine Learning*, PMLR, 2019, pp. 2415–2423.
- [76] Y. Azulay, E. Treister, Multigrid-augmented deep learning preconditioners for the helmholtz equation, *arXiv preprint arXiv:2203.11025* (2022).
- [77] N. Rahaman, A. Baratin, D. Arpit, F. Draxler, M. Lin, F. Hamprecht, Y. Bengio, A. Courville, On the spectral bias of neural networks, in: *International Conference on Machine Learning*, PMLR, 2019, pp. 5301–5310.

## **Acknowledgements**

This work is supported by the DOE PhILMs project (No. de-sc0019453), the MURI-AFOSR FA9550-20-1-0358 projects, and the DARPA HR00112290029 project.

## Supplementary Information

### *Section S1. Review of Numerical Methods for Linear Systems*

#### *Section S1A. Jacobi and Gauss-Seidel Methods*

We briefly review Jacobi and Gauss-Seidel methods. Through diverse discretization methods (such as finite difference and finite element), solving differential equations can be converted to solving linear equations. We seek  $\mathbf{u} \in \mathbb{R}^n$  in the linear system  $\mathbf{A}\mathbf{u} = \mathbf{f}$  ( $\mathbf{A} \in \mathbb{R}^{n \times n}$  is invertible,  $\mathbf{f} \in \mathbb{R}^n$ ). Splitting  $\mathbf{A} = \mathbf{M} + \mathbf{N}$  where  $\mathbf{M}$  is invertible, we get  $\mathbf{u} = -\mathbf{M}^{-1}\mathbf{N}\mathbf{u} + \mathbf{M}^{-1}\mathbf{f}$ . This yields the iteration

$$\mathbf{u}^{(k+1)} = -\mathbf{M}^{-1}\mathbf{N}\mathbf{u}^{(k)} + \mathbf{M}^{-1}\mathbf{f}. \quad (\text{S1})$$

The Jacobi method and the Gauss-Seidel method define  $\mathbf{M}$  and  $\mathbf{N}$  as

$$\text{Jacobi: } \mathbf{M} = \mathbf{D}, \mathbf{N} = \mathbf{L} + \mathbf{U}, \quad (\text{S2})$$

$$\text{Gauss-Seidel: } \mathbf{M} = \mathbf{D} + \mathbf{L}, \mathbf{N} = \mathbf{U}, \quad (\text{S3})$$

where  $\mathbf{L}$ ,  $\mathbf{D}$ ,  $\mathbf{U}$  are the strictly lower triangular, diagonal, and strictly upper triangular components of  $\mathbf{A}$ , respectively, so that  $\mathbf{A} = \mathbf{L} + \mathbf{D} + \mathbf{U}$ . For the Jacobi method, the weighted (damped) version of Eq. S1 is often adopted for better convergence properties, which is defined by

$$\mathbf{u}^{(k+1)} = (1 - \omega)\mathbf{u}^{(k)} - \omega\mathbf{M}^{-1}\mathbf{N}\mathbf{u}^{(k)} + \omega\mathbf{M}^{-1}\mathbf{f} \quad (\text{S4a})$$

$$= (1 - \omega)\mathbf{u}^{(k)} - \omega\mathbf{D}^{-1}(\mathbf{L} + \mathbf{U})\mathbf{u}^{(k)} + \omega\mathbf{D}^{-1}\mathbf{f}, \quad (\text{S4b})$$

where  $\omega$  is the damping parameter. The algorithm is shown in Alg. S1. During the iterations, for an approximate solution  $\mathbf{u}^{(k)}$ , we define the residual and the error as

$$\mathbf{r}^{(k)} = \mathbf{f} - \mathbf{A}\mathbf{u}^{(k)}, \quad (\text{S5a})$$

$$\mathbf{e}^{(k)} = \mathbf{u}^{(k)} - \mathbf{u}, \quad (\text{S5b})$$

respectively, where  $\mathbf{u}$  is the true solution and  $\mathbf{r}^{(k)}$  and  $\mathbf{e}^{(k)}$  satisfy  $\mathbf{A}\mathbf{e}^{(k)} = \mathbf{r}^{(k)}$ . The evolution of error is given by

$$\mathbf{e}^{(k+1)} = [(1 - \omega)\mathbf{I} + \omega\mathbf{M}^{-1}\mathbf{A}]\mathbf{e}^{(k)} \quad (\text{S6a})$$

$$:= \mathbf{G}_\omega \mathbf{e}^{(k)}, \quad (\text{S6b})$$

where  $\mathbf{G}_\omega$  is the amplification matrix, which characterizes how the error vector evolves through iterations.

Based on an eigenvalue analysis of  $\mathbf{G}_\omega$  in Eq. S6b, we analyze the convergence properties of the damped Jacobi method for different modes in the error  $\mathbf{e}^{(k)}$  (i.e., eigenvectors of  $\mathbf{G}_\omega$ ). We expand the error  $\mathbf{e}^{(k)}$  as

$$\mathbf{e}^{(k)} = \sum_{j=1}^n e_j^{(k)} \boldsymbol{\phi}_j = \sum_{j=1}^n \lambda_j^n e_j^{(0)} \boldsymbol{\phi}_j, \quad (\text{S7})$$

where  $\{\lambda_j\}_{j=1}^n$ ,  $\{\boldsymbol{\phi}_j\}_{j=1}^n$  are the eigenvalues and eigenvectors of  $\mathbf{G}_\omega$ , respectively;  $e_j^{(k)}$  is the coefficient of mode  $\boldsymbol{\phi}_j$  in the error  $\mathbf{e}^{(k)}$ . For convenience, we sort  $\{\lambda_j\}_{j=1}^n$  and  $\{\boldsymbol{\phi}_j\}_{j=1}^n$  by the frequencies of  $\boldsymbol{\phi}_j$  in ascending order, so that  $\boldsymbol{\phi}_1$  corresponds to the lowest-frequency mode and  $\boldsymbol{\phi}_n$  corresponds to the highest-frequency mode. According to Eq. S7, the method converges if and only if  $\max_j |\lambda_j| < 1$ , and the convergence rate is dominated by  $\max_j |\lambda_j|$ . For the Poisson equation defined in Eq. 4, the damped Jacobi solver yields  $\max_j |\lambda_j| = |\lambda_1| < 1$ , making the iterative solution converge. For the Helmholtz equation defined in Eq. 5 with sufficiently large  $k(x)$ ,  $\max_j |\lambda_j| = |\lambda_1| > 1$ , making the iterative solution diverge.

### *Section S1B. Multigrid Methods*

To address the issue of slow convergence, multigrid methods have been proposed and widely applied in recent decades. The essence is to update the approximate solution through nested iterations in multiple grids. For a large linear system, one maps the problem into a coarser grid in a recursive approach, through which the low-frequency modes in the original grid becomes relatively high-frequency for the coarse grid, hence

---

**Algorithm S1** The (Damped) Jacobi Solver and the Gauss-Seidel Solver

---

**function** NUMERICAL\_SOLVER( $\mathbf{A}^h, \mathbf{f}^h$ )

$\mathbf{v}^h \leftarrow \mathbf{0}^h$  ▷ initial guess of the solution

$k_{\text{it}} \leftarrow 1$

**while**  $k_{\text{it}} \leq n_{\text{it}}$  and not converged **do**

$\mathbf{r}^h \leftarrow \mathbf{f}^h - \mathbf{A}^h \mathbf{v}^h$

**if** using damped Jacobi **then**

$\mathbf{v}^h \leftarrow \text{DAMPED\_JACOBI}(\mathbf{A}^h, \mathbf{f}^h, \mathbf{v}^h)$

**else if** using Gauss-Seidel **then**

$\mathbf{v}^h \leftarrow \text{GAUSS\_SEIDEL}(\mathbf{A}^h, \mathbf{f}^h, \mathbf{v}^h)$

**end if**

$k_{\text{it}} \leftarrow k_{\text{it}} + 1$

**end while**

**return**  $\mathbf{v}^h$

**end function**

▷ main function of the (damped) Jacobi and Gauss-Seidel solvers

**function** DAMPED\_JACOBI( $\mathbf{A}^h, \mathbf{f}^h, \mathbf{v}^h$ )

$\mathbf{v}^h \leftarrow (1 - \omega)\mathbf{v}^h - \omega(\mathbf{D}^h)^{-1}(\mathbf{L}^h + \mathbf{U}^h)\mathbf{v}^h + \omega(\mathbf{D}^h)^{-1}\mathbf{f}^h$

**return**  $\mathbf{v}^h$

**end function**

▷ one iteration of the damped Jacobi method

**function** GAUSS\_SEIDEL( $\mathbf{A}^h, \mathbf{f}^h, \mathbf{v}^h$ )

$\mathbf{v}^h \leftarrow -(\mathbf{L}^h + \mathbf{D}^h)^{-1}\mathbf{U}^h\mathbf{v}^h + (\mathbf{L}^h + \mathbf{D}^h)^{-1}\mathbf{f}^h$

**return**  $\mathbf{v}^h$

**end function**

▷ one iteration of the Gauss-Seidel method

---

converging significantly faster than solving the problem using the original grid. A typical multigrid V-cycle algorithm for solving  $\mathbf{A}^h \mathbf{u}^h = \mathbf{f}^h$  with (damped) Jacobi relaxation is summarized in Algorithm S2.

---

**Algorithm S2** Multigrid V-Cycle Algorithm with (Damped) Jacobi Relaxation

---

**function** MULTIGRID\_SOLVER( $\mathbf{A}^h, \mathbf{f}^h$ )

$\mathbf{v}^h \leftarrow \mathbf{0}^h$  ▷ initial guess of the solution

$k_v \leftarrow 1$

**while**  $k_v \leq n_v$  and not converged **do**

$\mathbf{r}^h \leftarrow \mathbf{f}^h - \mathbf{A}^h \mathbf{v}^h$

$\mathbf{v}^h \leftarrow \text{V\_CYCLE}(\mathbf{A}^h, \mathbf{f}^h, \mathbf{v}^h)$

$k_v \leftarrow k_v + 1$

**end while**

**return**  $\mathbf{v}^h$

**end function**

▷ main function of the multigrid V-cycle algorithm

**function** V\_CYCLE( $\mathbf{A}^h, \mathbf{f}^h, \mathbf{v}^h$ )

Loop  $n_{it}$  times  $\mathbf{v}^h = \text{DAMPED\_JACOBI}(\mathbf{A}^h, \mathbf{f}^h, \mathbf{v}^h)$  ▷ see Alg. S1

**if**  $\Omega^h$  is not the coarsest grid **then**

$\mathbf{A}^{2h}, \mathbf{f}^{2h} \leftarrow \text{RESTRICTION}(\mathbf{A}^h), \text{RESTRICTION}(\mathbf{f}^h - \mathbf{A}^h \mathbf{v}^h)$

$\mathbf{v}^{2h} \leftarrow \text{V\_CYCLE}(\mathbf{A}^{2h}, \mathbf{f}^{2h}, \mathbf{0}^{2h})$

$\mathbf{v}^h \leftarrow \mathbf{v}^h + \text{PROLONGATION}(\mathbf{v}^{2h})$

**end if**

Loop  $n_{it}$  times  $\mathbf{v}^h = \text{DAMPED\_JACOBI}(\mathbf{A}^h, \mathbf{f}^h, \mathbf{v}^h)$

**return**  $\mathbf{v}^h$

**end function**

▷ one V-Cycle

---

Multigrid methods have been shown to work for problems such as the Poisson equation,



where the left-hand-side matrix  $\mathbf{A}^h$  is positive definite. However, there exists a wide class of problems where  $\mathbf{A}$  is not positive definite. As a result, yielding  $\max_j |\lambda_j| > 1$  so that the multigrid method based on Jacobi relaxations diverges.

*Section S2. General Summary of DeepONet*

DeepONet approximates operators, i.e., the mapping from functions to functions. We define the target nonlinear operator as  $\mathcal{G} : v \mapsto u$ , where  $v : \mathbf{x} \mapsto v(\mathbf{x}) \in \mathbb{R}$  and  $u : \mathbf{y} \mapsto u(\mathbf{y}) \in \mathbb{R}$  are the input and output functions that are defined for  $\mathbf{x} \in D \subset \mathbb{R}^d$  and  $\mathbf{y} \in D' \subset \mathbb{R}^{d'}$ , respectively. The architecture of a DeepONet is illustrated in Fig S1. The DeepONet comprises of two subnetworks, namely, a branch network and a trunk network. To approximate  $u(\mathbf{y}) = \mathcal{G}(v)(\mathbf{y})$  for  $\mathbf{y} \in D'$ , the branch network takes as input  $[v(\mathbf{x}^{(1)}), v(\mathbf{x}^{(2)}), \dots, v(\mathbf{x}^{(m)})]^T$ , i.e., the evaluation of function  $v$  at  $\mathbf{x}^{(1)}, \mathbf{x}^{(2)}, \dots, \mathbf{x}^{(m)} \in D$ ; the trunk network takes  $\mathbf{y} \in D'$  as input. Branch network and trunk network yield outputs  $[b^{(1)}, b^{(2)}, \dots, b^{(p)}]^T$  and  $[t^{(1)}, t^{(2)}, \dots, t^{(p)}]^T$ , respectively. The inner product of these two vectors is the approximation of  $\mathcal{G}(v)(\mathbf{y})$  as the final output of the DeepONet. Complete details regarding DeepONet are explained in the original publication [35].

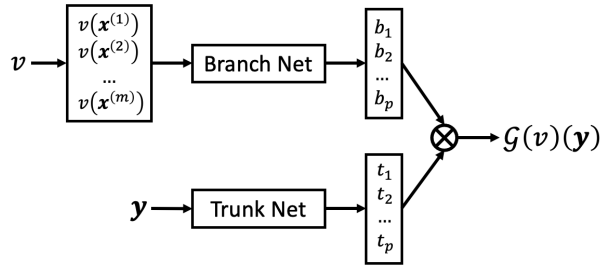


Figure S1: **Architecture of a DeepONet.** The DeepONet learns the operator  $\mathcal{G}$  that maps the input function  $v$  into the output function  $u := \mathcal{G}(v)$ . The branch network takes as input  $[v(\mathbf{x}^{(1)}), v(\mathbf{x}^{(2)}), \dots, v(\mathbf{x}^{(m)})]^T$ , i.e., the evaluation of function  $v$  at  $\mathbf{x}^{(1)}, \mathbf{x}^{(2)}, \dots, \mathbf{x}^{(m)}$ ; the trunk network takes  $\mathbf{y}$  as input. Branch network and trunk network yield outputs  $[b^{(1)}, b^{(2)}, \dots, b^{(p)}]^T$  and  $[t^{(1)}, t^{(2)}, \dots, t^{(p)}]^T$ , respectively. The inner product of these two vectors (plus a trainable bias) is the approximation of  $\mathcal{G}(v)(\mathbf{y})$  as the final output of the DeepONet.

Section S3. Technical Details

Section S3A Pseudo-code of Algorithms

---

**Algorithm S3** HINTS-Jacobi

---

```
function HINTS_JACOBI( $k(\mathbf{x}), f(\mathbf{x}), \text{PDE}$ )  
   $\mathbf{A}^h, \mathbf{f}^h = \text{DISCRETIZE}(k(\mathbf{x}), f(\mathbf{x}), \text{PDE})$     ▷ discretization; to solve  $\mathbf{v}^h = (\mathbf{A}^h)^{-1}\mathbf{f}^h$   
   $\mathbf{v}^h \leftarrow \mathbf{0}^h$                                 ▷ initial guess of the solution  
   $k_{\text{it}} \leftarrow 1$   
  while  $k_{\text{it}} \leq n_{\text{it}}$  and not converged do  
     $\mathbf{r}^h \leftarrow \mathbf{f}^h - \mathbf{A}^h \mathbf{v}^h$   
    if  $k_{\text{it}} \bmod n_r = 0$  then                    ▷ condition for invoking DeepONet  
       $r(\mathbf{x}) = \text{REVERSE\_DISCRETIZE}(\mathbf{r}^h)$           ▷ see Section S3E  
       $\delta \mathbf{v}^h (= \delta v(\mathbf{x})) \leftarrow \text{DEEPONET}(k(\mathbf{x}), r(\mathbf{x}))$   
       $\mathbf{v}^h \leftarrow \mathbf{v} + \delta \mathbf{v}^h$   
    else  
       $\mathbf{v}^h \leftarrow \text{DAMPED\_JACOBI}(\mathbf{A}^h, \mathbf{f}^h, \mathbf{v}^h)$     ▷ see Alg. S1  
      (or equivalently:  $\mathbf{v}^h \leftarrow \mathbf{v}^h + \text{DAMPED\_JACOBI}(\mathbf{A}^h, \mathbf{r}^h, \mathbf{0}^h)$ )  
    end if  
     $k_{\text{it}} \leftarrow k_{\text{it}} + 1$   
  end while  
  return  $\mathbf{v}^h (= v(\mathbf{x}))$   
end function
```

---

---

**Algorithm S4** HINTS-MG with V-cycle and Jacobi Relaxation

---

**function** HINTS\_MG( $k(\mathbf{x})$ ,  $f(\mathbf{x})$ , PDE) $\mathbf{A}^h, \mathbf{f}^h = \text{DISCRETIZE}(k(\mathbf{x}), f(\mathbf{x}), \text{PDE})$  $\mathbf{v}^h \leftarrow \mathbf{0}^h$  $k_v \leftarrow 1$ **while**  $k_v \leq n_v$  and not converged **do** $\mathbf{v}^h = \text{HINTS\_V\_CYCLE}(\mathbf{A}^h, \mathbf{f}^h, \mathbf{v}^h, k(\mathbf{x}))$ **end while****end function**

▷ main function

**function** HINTS\_V\_CYCLE( $\mathbf{A}^h, \mathbf{f}^h, \mathbf{v}^h, k(\mathbf{x})$ ) $\mathbf{v}^h = \text{HINTS\_JACOBI\_DISCRETE}(\mathbf{A}^h, \mathbf{f}^h, \mathbf{v}^h, k(\mathbf{x}))$ 

▷ Modified Alg. S3 without the first discretization step

**if**  $\Omega^h$  is not the coarsest grid **then** $\mathbf{A}^{2h}, \mathbf{f}^{2h} \leftarrow \text{RESTRICTION}(\mathbf{A}^h), \text{RESTRICTION}(\mathbf{f}^h - \mathbf{A}^h \mathbf{v}^h)$  $\mathbf{v}^{2h} \leftarrow \text{HINTS\_V\_CYCLE}(\mathbf{A}^{2h}, \mathbf{f}^{2h}, \mathbf{0}^{2h}, k(\mathbf{x}))$  $\mathbf{v}^h \leftarrow \mathbf{v}^h + \text{PROLONGATION}(\mathbf{v}^{2h})$ **end if** $\mathbf{v}^h = \text{HINTS\_JACOBI\_DISCRETE}(\mathbf{A}^h, \mathbf{f}^h, \mathbf{v}^h, k(\mathbf{x}))$  $k_v \leftarrow k_v + 1$ **return**  $\mathbf{v}^h$ **end function**▷ a single V-Cycle in HINTS-MG

---

*Section S3B. Discretization of Differential Equation*

We use the finite element method to discretize the 1D Poisson equation (Eq. 4). The computational domain  $\Omega = (0, 1)$  is partitioned into  $n = 30$  linear elements, except in Fig. S5 where  $n = 15, 45, 60$ .

For the 2D Poisson equation, we use the finite element method to discretize the domain into linear triangular elements (see the first panel in Fig. 5A). The mesh is generated using MATLAB. The side lengths for elements far from the corner  $(0, 0)$  are no larger than 0.05, while those for elements near the corner are 0.005. In total, there are 450 nodes and 802 elements in the domain.

For the  $d$ -dimensional ( $d \in \{1, 2, 3\}$ ) Helmholtz equation (Eq. 5), we discretize the domain  $\Omega = (0, 1)^d$  into  $n = 30, 32^2, 16^3$  Cartesian grids, respectively.

### Section S3C. Data Generation

The input data  $(k(\mathbf{x}), f(\mathbf{x}))$  for training and testing cases are generated using Gaussian random fields with means  $\mathbb{E}k(\mathbf{x}) = k_0 (> 0)$ ,  $\mathbb{E}f(\mathbf{x}) = 0$  and covariances

$$\text{Cov}(k(\mathbf{x}_1), k(\mathbf{x}_2)) = \sigma_k^2 \exp\left(-\frac{\|\mathbf{x}_1 - \mathbf{x}_2\|^2}{2l_k^2}\right); \quad (\text{S8})$$

$$\text{Cov}(f(\mathbf{x}_1), f(\mathbf{x}_2)) = \sigma_f^2 \exp\left(-\frac{\|\mathbf{x}_1 - \mathbf{x}_2\|^2}{2l_f^2}\right). \quad (\text{S9})$$

In addition, we only consider  $k(\mathbf{x})$  satisfying  $k(\mathbf{x}) > k_{\min}$ . The choices of  $k_0, k_{\min}, \sigma_k, l_k, \sigma_f, l_f$  are listed in Table S1.

Case	$k_0$	$k_{\min}$	$\sigma_k$	$l_k$	$\sigma_f$	$l_f$
1D Poisson	1.0	0.3	0.3	0.1	1.0	0.1
1D Helmholtz	8.0	3.0	2.0	0.2	1.0	0.1
2D Poisson (L-shaped)	1.0	0.3	0.3	0.1	1.0	0.1
2D Helmholtz	6.0	3.0	0.5	0.3	1.0	0.1
3D Helmholtz*	6.0	3.0	0.5	0.5	1.0	0.1

Table S1: **Parameters for Generating Training Data.** \*The parameters shown are for test data. For the training data,  $k_0 = 6.0, k_{\min} = 0.3, \sigma_k = 0.2, l_k = 0.1, \sigma_f = 0.1, l_f = 0.2$ .

After  $(k(\mathbf{x}), f(\mathbf{x}))$  are generated, we solve  $u(\mathbf{x})$  using standard numerical solvers. As an example, the generated training data for the 1D Poisson equation is shown in

Section S4A. For all the Helmholtz cases, these choices of  $k(x)$  ensure the indefiniteness of the system.

*Section S3D. DeepONet Architecture*

DeepONet takes the input function  $k(\mathbf{x})$  and  $f(\mathbf{x})$  in the forms of  $[k(\mathbf{x}_0), k(\mathbf{x}_1), \dots, k(\mathbf{x}_{n_D})]^\top$  and  $[f(\mathbf{x}_0), f(\mathbf{x}_1), \dots, f(\mathbf{x}_{n_D})]^\top$ , respectively, where  $\{\mathbf{x}_i\}_{i=0}^{n_D}$  are uniform grid points in  $\Omega$ . For 1D cases, the size of the branch network is  $[62, 60, 60, 60]$ , where we concatenate  $k(x)$  and  $f(x)$ , resulting in the input dimension  $2(n_D + 1) = 62$ ; the dimension of the trunk network is  $[1, 60, 60, 60]$ . We train the DeepONet for 10,000 epochs with an initial learning rate  $10^{-3}$ , a decay rate of 50% per 5,000 epochs, and a mini-batch size of 500. See the training results for the 1D Poisson equation in Section S4A.

For the 2D cases, the branch net is a combination of a CNN (input dimension  $31 \times 31$ , number of channels  $[2, 40, 60, 100, 180]$ , kernel size  $3 \times 3$ , stride 2, the number of channels of the input 2 comes from the concatenation of  $k(x)$  and  $f(x)$ ) and dense NN (dimension  $[180, 80, 80]$ ). The dimension of the trunk network is  $[2, 80, 80, 80]$ . We train the DeepONet for 25,000 epochs with a fixed learning rate  $10^{-4}$ , and a mini-batch size of 10,000.

For the 3D Helmholtz case, the branch net is a combination of a 3D CNN (input dimension  $31 \times 31 \times 31$ , number of channels  $[2, 40, 60, 100]$ , kernel size  $3 \times 3 \times 3$ , stride 2) and dense NN (dimension  $[100, 80, 80]$ ). The dimension of the trunk network is  $[3, 80, 80, 80]$ .  $k(x, y)$  and  $f(x, y)$ , each with size  $14 \times 14 \times 14$ , are concatenated as two input channels in the branch network. We train the DeepONet for 25,000 epochs with a learning rate  $10^{-4}$ , and a mini-batch size of 10,000.

For all the cases, the activation function is the Rectified Linear Unit (ReLU) for branch networks (excluding the last layer that has no activation function) and Hyperbolic Tangent (Tanh) for trunk networks (including the last layer). The loss function is defined

by

$$\mathcal{L} = \frac{1}{N(n_D + 1)} \sum_{j=1}^N \sum_{i=0}^{n_D} \frac{(\hat{u}_{(j)}(\mathbf{x}_i) - u_{(j)}(\mathbf{x}_i))^2}{\varepsilon + |u_{(j)}(x)|^\alpha}, \quad (\text{S10})$$

where  $N$  is the size of training data,  $(\cdot)_{(j)}$  refers to quantities from the  $j$ th training sample,  $(\hat{\cdot})$  refers to the prediction,  $\alpha$  is a parameter, and  $\varepsilon$  is a small number for preventing zero denominator when  $\alpha \neq 0$ . For the 1D Poisson equation,  $\alpha = 0$ , making the loss function the mean squared error. For the 1D Helmholtz equation,  $\alpha = 1$ . For other cases,  $\alpha = 2$ . When  $u(x)$  changes dramatically across different samples, a positive value of  $\alpha$  yields weights that are biased appropriately towards  $u(x)$  with smaller magnitudes.

### *Section S3E. Reversion of Residuals*

Standard numerical solvers deal with discretized, matrix- and vector-form representation of the system, such as  $\mathbf{A}^h$ ,  $\mathbf{f}^h$  or  $\mathbf{r}^h$ , and  $\mathbf{u}^h$ . On the other hand, the DeepONet solver deals with the function-form representation of the system, such as  $k(\mathbf{x})$ ,  $f(\mathbf{x})$  or  $r(\mathbf{x})$ , and  $u(\mathbf{x})$  (more specifically, the discrete evaluation of these functions).

We now explain in detail how to bridge the gap between these two representations. First,  $u(\mathbf{x})$  and  $\mathbf{u}^h$  are essentially the same quantities (up to  $n \neq n_D$  which simply needs an interpolation). The only issue is in terms of the translation between  $\mathbf{f}^h$  ( $\mathbf{r}^h$ ) and  $f(\mathbf{x})$  ( $r(\mathbf{x})$ ). For all cases except the 2D Poisson equation in an L-shaped domain, the grids are uniform, so that  $\mathbf{f}^h$  and  $f(\mathbf{x})$  are possibly different only in terms of a constant of the grid size. We always absorb this constant into  $\mathbf{A}^h$ , so that  $\mathbf{f}^h$  and  $f(\mathbf{x})$  are equivalent (similar to  $u(\mathbf{x})$  and  $\mathbf{u}^h$ ). For the case of the 2D Poisson equation in an L-shaped domain, due to the nonuniform meshes, we need to explicitly calculate  $f(\mathbf{x})$  from  $\mathbf{f}^h$ . We approximately calculate  $f(\mathbf{x}_i)$ , where  $\mathbf{x}_i$  is node  $i$ , by

$$f(\mathbf{x}_i) = \frac{3f_i^h}{\sum_j A_j}, \quad (\text{S11})$$

where  $f_i^h$  is the component  $i$  of  $\mathbf{f}^h$ ,  $A_j$  is the area of element  $j$ , and the summation is calculated for all elements that include node  $i$ . While this calculation is approximate, it is

only used for the DeepONet inference that essentially provides an approximate solution. Hence, such approximation does not influence the overall performance of HINTS.

*Section S4. Additional Results*

*Section S4A. 1D Poisson*

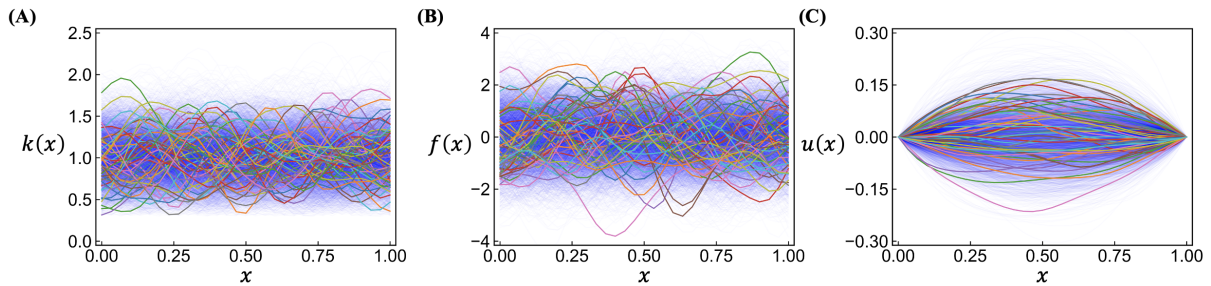


Figure S2: DeepONet Training Data for 1D Poisson Equation.

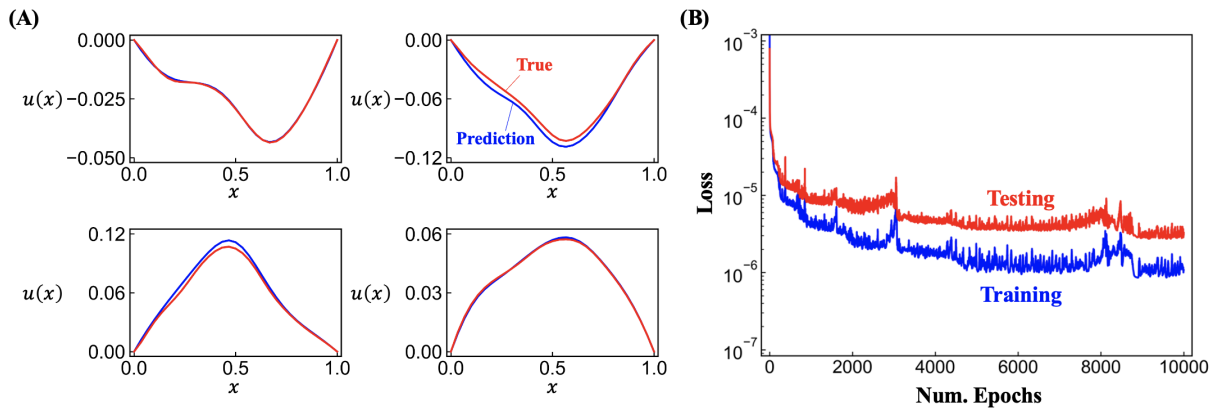


Figure S3: Results of DeepONet Training for 1D Poisson Equation. (A) Comparison of the predicted and true solutions  $u(x)$  for four typical test cases. (B) Loss function for training and testing.

	Mean	Std.	Min	Max
Convergence Rate $\mu (\times 10^{-2})$	6.8	0.65	5.16	8.72

Table S2: Results of 1D Poisson Equation for 100 Test Cases.

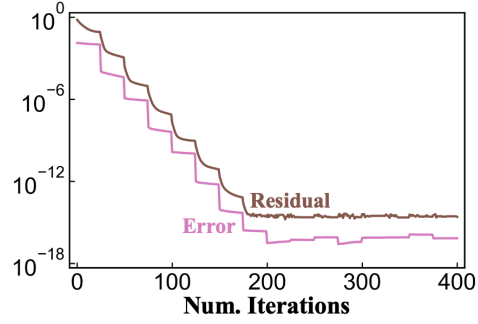


Figure S4: **Results of 1D Poisson Equation Solved with HINTS-GS.**

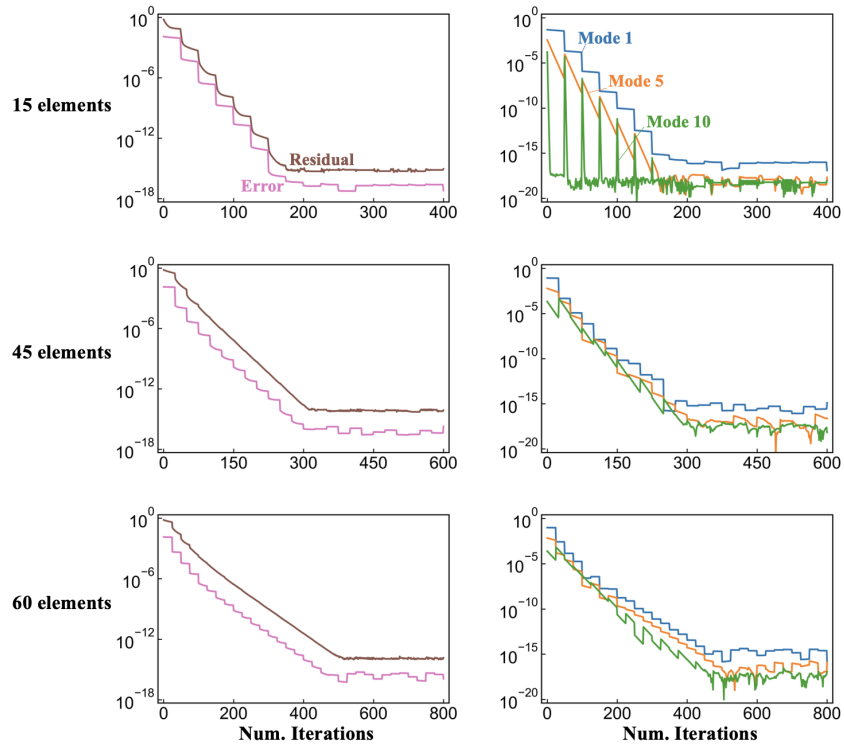


Figure S5: **Results of 1D Poisson Equation with Mismatching Discretization.** We use the identical DeepONet to the one in the main text (trained with  $n_D = 30$ ) to solve equations discretized with different numbers of intervals  $n = 15, 45, 60$ . The first column and the second column shows the histories of the norms of residual and error (first column) and the mode-wise error (second column), respectively.



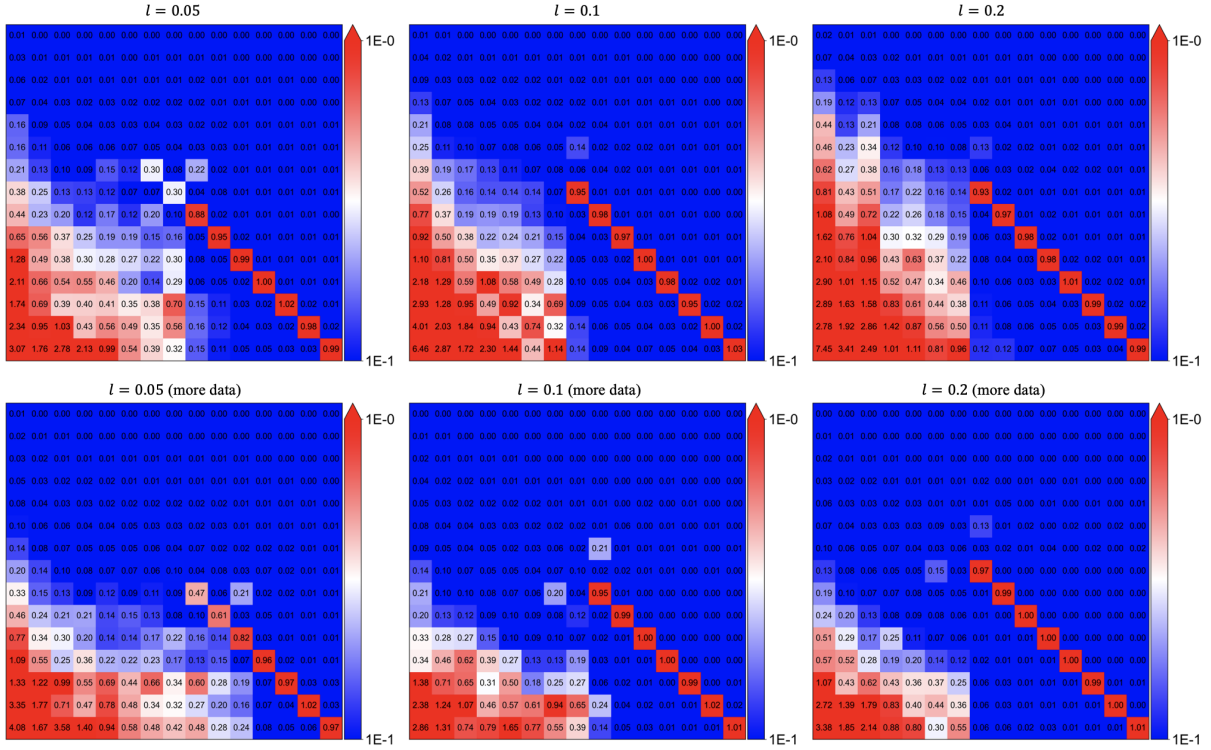


Figure S6: Mode-wise Performance of the Trained DeepONet for 1D Poisson Equation with Different Training Setups. See Fig. 3A for the results of the standard setup, which is repeated herein in the first row, the second column. The first row corresponds to 5,000 training cases, the same as in the main text; the second row corresponds to 10,000 training cases. The three columns correspond to training data generated from Gaussian random field with correlation lengths  $l = 0.05, 0.1, 0.2$ , respectively, where  $l = 0.1$  is the same as in the main text.

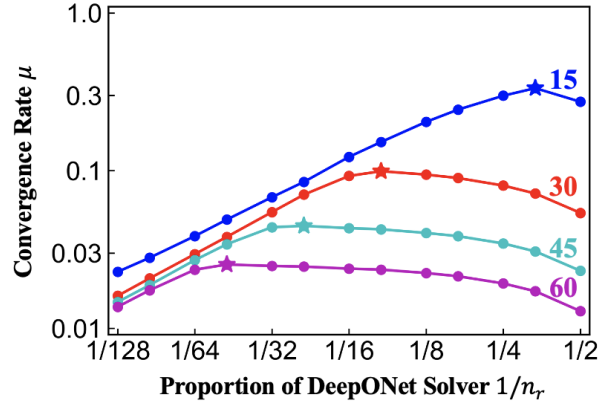


Figure S7: **Convergence Rate for Different Fractions of DeepONet in Numerical Problems with Different Numbers of Sub-intervals.** The four lines correspond to numbers of sub-intervals  $n = 15, 30, 45, 60$ .

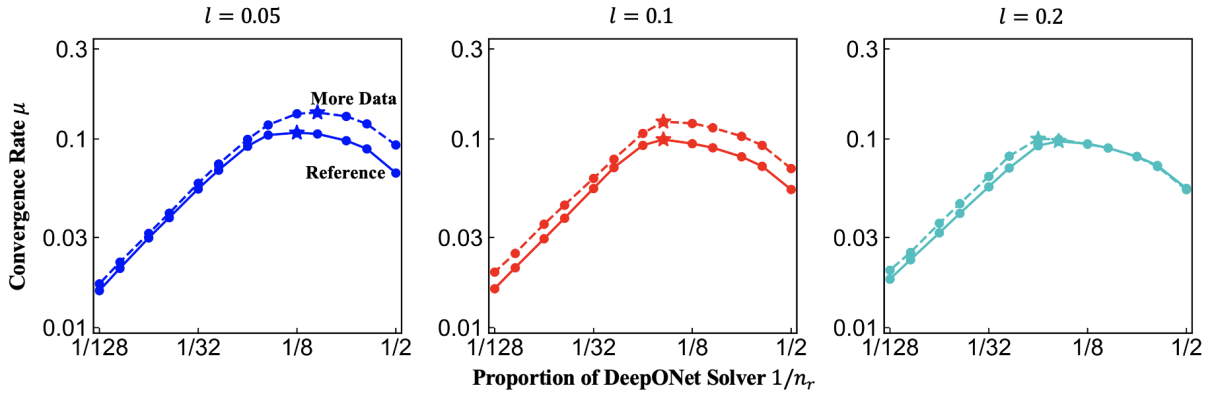


Figure S8: **Convergence Rate for Different Fractions of DeepONet with Different Training Strategies of DeepONet.** We consider different correlation lengths ( $l = 0.05, 0.1, 0.2$ ) in the Gaussian random field for generating the training data, as well as different size of training data (5,000 or 10,000 cases).

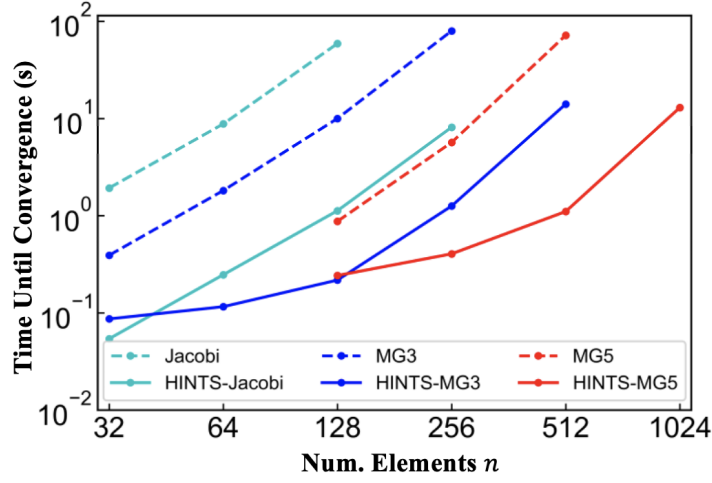


Figure S9: **Computational Cost of Different Methods for 1D Poisson Equation.** All multigrid (MG) methods use damped Jacobi relaxation. MG3 and HINTS-MG3 use three grid levels, and MG5 and HINTS-MG5 use five grid levels.

Section S4B. 2D Helmholtz

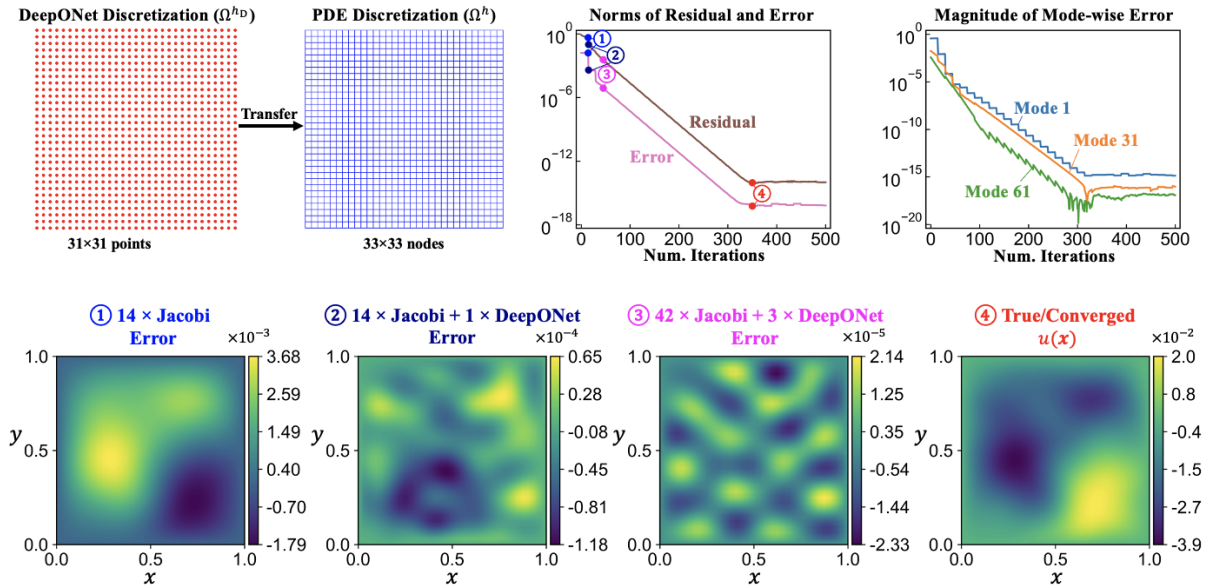


Figure S10: **Results of 2D Helmholtz Equation.**

*Section S4C. 3D Helmholtz*

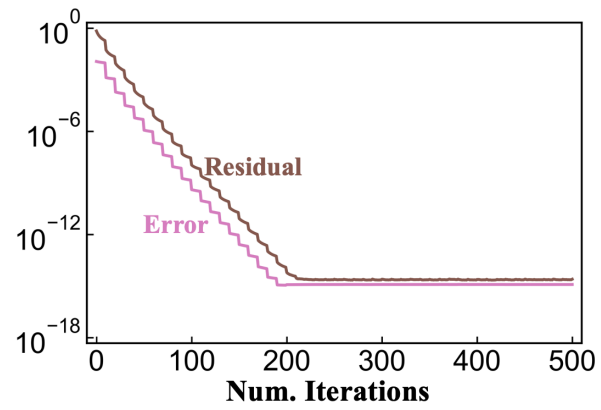


Figure S11: Results of 3D Helmholtz Equation Solved with HINTS-GS.

Section S5. Definitions of Notations

Math Symbol	Description
$x(\mathbf{x})$	Spatial coordinates for one- (multi-) dimensional problems
$\mathbf{A}^h$	Left-hand-side matrix in the linear system ( $\in \mathbb{R}^{n \times n}$ ; with discretization $h$ )
$\mathbf{L}^h$	Strictly lower triangular part of $\mathbf{A}^h$
$\mathbf{D}^h$	Diagonal part of $\mathbf{A}^h$
$\mathbf{U}^h$	Strictly upper triangular part of $\mathbf{A}^h$
$\mathbf{M}^h, \mathbf{N}^h$	Two matrices split from $\mathbf{A}^h$ (see Eqs. S1- S3)
$\mathbf{f}^h$	Right-hand-side loading vector in the linear system ( $\in \mathbb{R}^{n \times 1}$ ; with discretization $h$ )
$\mathbf{r}^h$	Residual vector
$\mathbf{e}^h$	Error vector
$\mathbf{u}^h$	True solution of linear system $\mathbf{A}^h \mathbf{u}^h = \mathbf{f}^h$
$\mathbf{v}^h$	Approximate solution of $\mathbf{u}^h$
$\delta \mathbf{v}^h$	Correction of $\mathbf{v}^h$ in an iteration
$\phi_i^h$	Eigenmode $i$ of $\mathbf{u}^h$
$(\cdot)^h$	Matrices/Vectors corresponding to the grid $\Omega^h$
$(\cdot)^{2h}$	Matrices/Vectors corresponding to the coarser grid $\Omega^{2h}$ (with respect to $\Omega^h$ )
$k = k(\mathbf{x})$	function parameterizing the differential equation (see Eq. 1a)
$f = f(\mathbf{x})$	function parameterizing the differential equation (see Eq. 1a)
$r = r(\mathbf{x})$	residual function
$u = u(\mathbf{x})$	True solution (function) of the differential equation (see Eqs. 1a-1b)
$v = v(\mathbf{x})$	Approximate solution (function) of $u(\mathbf{x})$
$\phi_i = \phi_i(\mathbf{x})$	Eigenmode $i$ of $u(\mathbf{x})$

Table S3: Notations in the Paper.

Math Symbol	Description
$l_k, l_f$	Correlation lengths of the Gaussian random field for generating $k(x)$ and $f(x)$
$N$	Number of training cases
$n$	Number of grids/elements/sub-intervals in the numerical problem
$n_D$	Number of grids/elements/sub-intervals for DeepONet training
$k_{it}$	The index of the current iteration in the numerical solver
$k_v$	The index of the current V-cycle in the multigrid solver
$(\cdot)^{(k_{it})}$	Matrices/Vectors in $k_{it}$ -th iteration
$n_{it}$	Number of total iterations in the numerical solver
$n_r$	Reciprocal of the proportion of DeepONet in HINTS (i.e., DeepONet-to-numerical ratio 1 : ( $n_r - 1$ ))
$n_v$	Number of V-cycles in multigrid methods
$n_{r1}$	Number of relaxation steps in each grid level of multigrid methods
$n_{cut}$	Number of modes that the DeepONet is able to predict accurately
$\mu$	Convergence rate (see Eq. 6)
$\mathcal{G}$	Operator that the DeepONet seeks to learn (see Eq. 2)
$\mathcal{L}_x$	Linear differential operator in Eq. 1a
$\mathcal{B}_x$	Boundary operator in Eq. 1b
$\Omega$	computational domain of the differential equation
$\Omega^{h_D}$	Discretized $\Omega$ for DeepONet
$\Omega^h$	Discretized $\Omega$ for the numerical problem
$\omega$	Damping parameter
$\alpha$	Parameter in the loss function (see Eq. S10)
$\hat{(\cdot)}$	Predicted value from DeepONet
$(\cdot)_{(j)}$	Quantity from the $j$ th training sample

Table S4: Notations in the Paper (Continued).